The Pennsylvania State University

The Graduate School

IMPACTS OF PART-TO-PART VARIABILITY ON GAS TURBINE BLADE COOLING

A Thesis in

Mechanical Engineering

by

Kelsey McCormack

Submitted in Partial Fulfillment

of the Requirements

for the Degree of

Master of Science

December 2023

The thesis of Kelsey McCormack will be reviewed and approved by the following:

Karen A. Thole
Distinguished Professor
Thesis Advisor

Reid A. Berdanier
Associate Research Professor

Robert Kunz
Associate Department Head for Graduate Studies
Professor of Mechanical Engineering

ABSTRACT

Gas turbine inlet temperatures continue to increase in an effort to improve efficiency. Therefore, effective cooling of hot section components is necessary to reduce deterioration and maintain part life. Despite the best efforts of engine designers, coolant flow blockages or degradation of thermal barrier coatings will nevertheless occur during operation and lead to increased surface temperatures that reduce blade life. This phenomenon is especially prevalent in environments where sand or other small particles are ingested into engines. Part-to-part manufacturing variations also lead to significant changes in geometry relative to design intent that impact the flow and cooling effectiveness of turbine components, even when the deviations are within defined tolerances.

This thesis examines part-to-part variations in geometry, flow, and cooling effectiveness for true scale turbine blades. A set of engine-run blades with varying levels of environmental deterioration was operated at engine-relevant conditions and surface temperature was measured using infrared thermography. These measurements were used to calculate cooling effectiveness and expected blade life. Blade flow parameter and cooling effectiveness were both high for blades operated in a benign environment, even though the benign run time blades had the highest run time of the blades measured. Blades operated in a harsh environment not only had lower cooling effectiveness, but also more variation in cooling effectiveness between blades. Film cooling trajectories were calculated for each set of blades tested, and showed that all engine-run blades had a significant reduction in maximum cooling effectiveness behind cooling holes with respect to a set of baseline blades. Cooling effectiveness values were then used to scale surface temperatures up to actual engine operating conditions extracted from the NASA E^3 program. While lifing curves from previous literature were able to predict blade temperatures for benign environment blades, surface temperature increased much more than expected for harsh operator blades.

A second study analyzed the flow performance and geometry of additively manufactured turbine blades with drilled film cooling holes. A benchtop flow rig was used to characterize flow through the full blade as well as isolated regions of the blade. While partial flow through specific regions of the blade did not match design intent, the total flow through the blade varied by less than 10% between the minimum and maximum flow blades at the design pressure ratio. Computed tomography scans were used to analyze the geometry of cooling features such as film cooling holes, crossover holes, turbulators, and pin fins. Shaped film cooling holes manufactured with a conventional electrical discharge machining (EDM) method were undersized throughout the entire cooling hole. A high-speed EDM method created holes that met design specifications in the metering section, but were also undersized at the hole exit. Additively manufactured features such as turbulators and pin fins were close to design intent shape and size, with the largest variations occurring on downskin surfaces that were unsupported during the build. Roughness was high on both internal and external blade surfaces, particularly for regions with the thinnest walls. This study demonstrated the viability of applying additively manufacturing and advanced hole drill methods to study new turbine cooling technologies at an accelerated timeline and reduced cost.

TABLE OF CONTENTS

LIST OF FIGURES

LIST OF TABLES

NOMENCLATURE

A	film cooling hole cross-sectional area
d	pin diameter
D	film cooling hole diameter
D_x	crossover hole diameter
D_h	hydraulic diameter (4A/p)
FP	flow parameter ($\dot{m}\sqrt{T_{in}}/P_{out}$)
ΔFP	percent change in flow parameter ($100 * (FP - FP_{ref}) / FP_{ref}$)
LE	leading edge
$\dot{m}$	mass flow rate
p	perimeter
P	absolute pressure
PR	pressure ratio (P_{in}/P_{out})
PS	pressure side
R_a	arithmetic mean roughness $\left(\frac{1}{n}\sum_{i=1}^{n}\lvert z_i - \mu\rvert\right)$
s'	path distance along cooling jet trajectory
SS	suction side
t_w	blade wall thickness
Δt	$(t - t_{baseline}) / (t_{max} - t_{baseline})$
T	temperature
TE	trailing edge
x'	axial distance downstream of cooling hole
X	global horizontal coordinate in image (pixels)
y'	radial distance downstream of cooling hole

Y	global vertical coordinate in image (pixels)

Greek

β	expansion angle
Δ	difference
ε_p	precision uncertainty
ϕ	overall effectiveness $(T_\infty-T_s) / (T_\infty-T_c)$

Subscripts

A	area-averaged
c	cooling air
d	design intent
in	channel inlet
fwd	forward
lat	lateral
max	maximum flow parameter
med	median flow parameter
min	minimum flow parameter
out	outlet
p	precision
s	blade surface
x	crossover hole
∞	mainstream

ACKNOWLEDGEMENTS

I would first like to thank Dr. Karen Thole for her guidance and support in my time at START. Additionally, I would like to thank Dr. Reid Berdanier for the mentorship you've provided throughout my time in graduate school. I am incredibly grateful for the opportunities you've both provided and for helping me to develop my skills as a researcher and engineer. The START students have been a life saver throughout my time here, and I greatly appreciate both the technical and moral support these past few years. Thank you as well to the START faculty and staff, whose support I greatly appreciate.

I would also like to thank Pratt & Whitney for their support throughout my time in graduate school. I have greatly appreciated their expertise and am very grateful for the amazing projects on which I have been able to work. Additionally, I would like to thank the Department of Energy and NASA for funding this research.[1]

To Thomas, I will be forever thankful for the love and support you have provided over the past few years. I could not have done this without you, and will always be grateful that START brought me to you. Lastly, thank you to my family for the endless encouragement in my journey to become an engineer. I am so incredibly grateful for everything you have done to make this possible.

[1] The author would like to acknowledge the support of the U.S. Department of Energy National Energy Technology Laboratory under award number DE-FE0025011, the NASA Aeronautics Research Mission Directorate (ARMD) University Leadership Initiative (ULI) under cooperative agreement number 80NSSC21M0068, and the NASA Aeronautics Research Mission Directorate (ARMD) Hybrid Thermally Efficient Core (HyTEC) Program under contract number 80GRC021CA008. Any opinions, findings, and conclusions or recommendations expressed in this material are those of the author and do not necessarily reflect the views of the National Aeronautics and Space Administration.

Chapter 1

Introduction

Gas turbines are commonly used for aircraft and industrial power generation applications. As gas turbine designers aim to increase turbine efficiency, turbine inlet temperatures have been steadily rising. This temperature rise poses a durability challenge for turbine designers, as the turbine inlet temperature has been higher than metal softening temperatures for decades. To cool components, air is diverted from the compressor section and inserted at other locations to ensure safe metal temperatures. A variety of cooling designs, both internal and external, have been developed and researched in great detail.

However, manufacturing constraints may place limitations on the types of carefully engineered cooling designs and their performance. Even small changes from design intent can have a large effect on the flow and heat transfer present in turbine blades. Additionally, these variations may be amplified when parts operate in engines and deteriorate or accumulate particle material. In sandy environments, a variety of deterioration mechanisms will decrease the performance and life of parts. The most common deterioration mechanisms involve either the deterioration of coatings and surfaces or blockages in cooling holes, preventing cooling flow from moving as intended. This thesis will discuss the impacts that manufacturing variations and engine deterioration have on turbine blade performance.

1.1 Part-to-Part Variability in Gas Turbines

While part-to-part variations are to be expected when manufacturing gas turbine components, these variations can have large impacts on performance. This is especially true for cooling features,

which are often small enough that even variations within defined tolerance can significantly alter the heat transfer and pressure loss through components. Whereas turbine airfoils are traditionally manufactured using single crystal casting, features such as film cooling holes are often drilled separately using electrical discharge machining (EDM). EDM uses a carefully controlled spark between an electrode and the component being machined to vaporize material and create a desired shape. Because these features are already so small, any changes in this manufacturing process will change the cooling hole shape and size.

As turbine blades operate in engines, they experience a variety of deterioration mechanisms that impact their thermal and aerodynamic performance. Thermal barrier coatings (TBC) are often used on parts to protect from hot main gas path air, but as the coating wears away the blade metal surface is more likely to be exposed to this hot air and reach higher temperatures. Additionally, particulates from the environment can be ingested into the engine and impact blade surfaces. Depending on the location that particles impact the surface, they can either deteriorate the TBC or enter and block cooling features. When cooling passages are blocked and cold air cannot reach the surface, the film cooling effectiveness greatly decreases.

Deterioration is more severe in harsh environments with high particulate levels. As more of these particulates are ingested into the engine, their impact further reduces flow and cooling effectiveness. Surface temperature increases of only 25° to 40° C can halve the life of a turbine blade [1–3], meaning the life of components in harsh environments with higher surface temperatures drastically decreases. It is therefore important to understand how cooling effectiveness changes for parts run in different environments around the world.

Additionally, the bulk of research on turbine components has focused on cast parts. In recent years, however, research into additive manufacturing (AM) of gas turbine components has grown significantly. AM has been used for novel designs of fuel injectors, tip shrouds, and even first or second stage turbine vanes. While material limitations due to the high temperatures and stresses on

rotating components prevent its use in turbine blades, it can instead be used for rapid prototyping to test new cooling designs at scaled conditions. The reduced costs and timeline to manufacture parts additively make it a great tool to advance cooling technologies more quickly and efficiently. While many additively manufactured cooling designs have been studied individually in coupons, there is little research analyzing how these designs print for relevant turbine geometries. Additionally, studying the effects of these deviations will provide a better understanding of how well AM blades can represent design intent parts in advancing turbine cooling technologies.

1.2 Objectives and Document Outline

This thesis will analyze the effects of part-to-part variations on turbine blade geometries, flow, and cooling effectiveness. One study investigated engine-run components, while the second study looked at additively manufactured parts with advanced hole drill methods. Chapter 2 covers flow and cooling effectiveness variations in engine-run components and was published at the ASME Turbo Expo 2023 conference, as well as being accepted to the Journal of Turbomachinery. Chapter 3 compared as-built additively manufactured blades with EDM film cooling holes to their design intent and analyzed the flow through these components. This study will be submitted to the ASME Turbo Expo 2024 conference and the Journal of Turbomachinery. Chapter 4 will summarize these two studies and provide recommendations for future research. The objective of this thesis is to provide an overview of how manufacturing variations and engine deterioration will affect the performance of turbine blades and to advance gas turbine cooling technologies.

Chapter 2

Quantifying Part-to-Part Flow Variations and Cooling Effectiveness in Engine-Run Blades

Abstract

As turbine inlet temperatures continue to increase for modern gas turbine engines, the lifing of hot section components operating in a range of environments is becoming increasingly challenging. Engine operations in harsh environments can cause a reduction in cooling capability leading to reduced blade life relative to existing experience. This study analyzes the effects of harsh environments on the deterioration of blade flow and cooling effectiveness in turbine blades by comparing three commercially-operated engines with varied operational times referenced against a baseline blade. Spatially-resolved surface temperatures measured using infrared thermography at high-speed rotating conditions were evaluated to determine variations in cooling effectiveness as a function of engine operation and blade-to-blade variability from the different commercial applications. Engine-run blades were found to have reduced flow as well as greater part-to-part variation when compared to baseline blades. Blade surface temperature measurements on the deteriorated operational blades indicated film cooling traces dissipated closer to the hole exit relative to baseline blades. Furthermore, the cooling effectiveness varied significantly even between blades from the same engines. The reduction in cooling effectiveness in the engine-run blades led to higher blade temperatures and significantly shorter component life, with some exhibiting as much as an 18% reduction in life compared to baseline blades. This knowledge allows lifing models to be developed toward predicting blade operational effects in harsh environments.

2.1 Introduction

Gas turbine designers continue to increase turbine inlet temperatures to improve efficiency resulting in flow temperatures well over 400°C hotter than the melting temperatures of metal components in the main gas path [1,2]. Although airfoil cooling designs, along with thermal barrier coatings, are able to protect hot gas path components throughout their intended life, vane and blade surfaces degrade differently because of environmental impacts. Over cycle times, airfoils experience spallation, erosion, hot corrosion, and particle deposition [3]. These deterioration mechanisms are particularly dramatic when operating in harsh environments with a significant density of particulates that are ingested into the engine.

Advanced cooling designs can protect components exposed to the hot gas path and extend part life. However, even in newly manufactured blades, part-to-part variations cause differences in cooling performance with respect to the design intent [4,5]. Compounded with environmental effects, manufacturing variability of components can lead to significant variability in engine operational times.

In this paper, spatially-resolved blade temperatures are measured and analyzed while operating at engine scale conditions to understand the effects of operating environments relative to a set of baseline blades. The blades examined in this study were operated in aircraft engines around the world experiencing varying levels of deterioration and, as a result, changes of overall cooling effectiveness. These blades were placed in a test turbine whereby spatially-resolved temperatures were measured using infrared thermography.

2.2 Literature Review

As blades operate over time, thermal barrier coatings (TBC) deteriorate and film cooling performance decreases. These coatings experience a variety of deterioration mechanisms [6], many of which lead to increased surface roughness [7,8] and external heat transfer [3,9–11]. Erosion and spallation commonly occur near cooling holes, which therefore affect the trajectory of the film in these regions [8–10]. In addition, particles have been shown to deposit on part surfaces or in cooling holes, causing blockages that increase heat transfer to the blade [11,12]. This deposition occurs most often at high temperatures and increased impingement angles, as well as for large particle sizes and high velocities [13,14].

Deterioration effects are compounded by manufacturing variability of turbine parts, which can also cause deviations in film cooling performance. Factors of the manufacturing process can lead to variations in blade geometries [4] and impact blade film cooling [5,15]. Depending upon the application method, often the TBC can partially block film cooling holes [7], leading to decreased cooling performance in newly manufactured parts [16,17]. This variability only worsens during engine operation.

Deterioration is accelerated for parts operating in harsh environments thereby shortening blade life. For example, Calcia-magnesia-alumina-silicate (CMAS) particles, sand, dirt, and other small particulates found commonly in certain parts of the world often cause significant damage to turbine hardware [18,19]. As a specific example, engines operated in the Vietnam War were removed from service after an average of 80 hours due to extreme compressor blade erosion [20]. Similarly, blades from Army rotorcrafts operated in Southwest Asia more recently showed significant damage due to CMAS attack and extreme deterioration [21]. The severity of this deterioration means that operating environment typically has an important effect on blade life, which differs from expected blade lifing per the design.

As further evidence of deterioration effects, Sidwell and Darmofal [22] found that an airline operating shorter flights with higher ambient temperatures had much shorter mean engine life compared to airlines operating at lower ambient temperatures. Investigations have predicted blade life to be reduced by 50% for temperature increases between 25° and 40° C [23–26]. These estimates were used by Knisely et al. [5], who showed how manufacturing differences affected flow and cooling effectiveness. Similar to the study reported in this paper, Knisely et al. used an infrared (IR) thermal imaging technique to measure blade surface temperatures and reported on the variability that can occur. These temperatures were then scaled to real engine values using data from the NASA E^3 engine [27], showing life reductions of up to 50% due to manufacturing variations alone. Similar methods to this study will be used in the present paper, but will be applied to engine-run deteriorated blades instead of newly manufactured blades.

While many papers have been discussed that analyzed turbine blade deterioration, only a few of these studies have used actual turbine hardware. Even fewer employ data collected from blades operating at engine-relevant conditions. In addition to the previously mentioned study by Knisely et al. [5], there have been other recent studies using IR thermography to spatially resolve blade surface temperatures in a rotating environment. Lemieux [28] and Markham et al. [29] both used IR cameras to measure temperatures inside of in-service gas turbines, while additional studies have used infrared cameras in rotating turbine rigs to view blade tips and endwalls [30–32].

Michaud et al. [33] used IR imaging to analyze the overall cooling effectiveness on engine-run nozzle guide vanes (NGVs) in an annular cascade . Both mid-life and end-of-life parts run in non-sandy environments were compared to new parts with the same geometries. They found that area-averaged overall cooling effectiveness decreased for engine-run parts, particularly on the pressure side and early suction side near the leading edge. End-of-life vanes were expected to have much higher surface temperature increases at engine conditions, by up to a 65° C on the pressure side. Their study also found that superposing the effects of individual deterioration features was

not able to accurately predict variations in cooling effectiveness, and that testing at engine-representative conditions is necessary to understand true performance. While this study provides important information on how parts can deteriorate over their lifetime, it does not compare variations in different operating environments, which the present paper will address.

The purpose of this study is to examine the effects of deterioration in harsh environments on overall cooling effectiveness and blade life. Our study is unique because the data presented compares both flow variations and overall effectiveness levels in engine-operated parts from both harsh and benign environments around the world. These variations were quantified for both different engine operational environments and different blades within the same engine. The use of IR thermography allowed for spatially-resolved temperature and cooling effectiveness measurements across the entire blade pressure and suction surfaces while operating at engine-relevant conditions. The focus of this paper is the data on the pressure side near the blade tip, as this location is often found to exhibit relatively hotter surface temperatures. These temperatures were then scaled to real-engine temperatures to calculate expected blade life.

2.3 Facility and Instrumentation

Testing for this study was carried out at the Steady Thermal Aero Research Turbine (START) Laboratory. START houses an open loop, continuous duration turbine test facility that operates at engine-relevant conditions matching Mach, Reynolds, Rotational Reynolds, and Biot numbers. Matching these non-dimensional parameters to that of an engine provides the ability to scale measured temperatures at test conditions to that of engine conditions. An overview of the facility can be seen in Figure 2.1. More information about this facility is described by Barringer et al. [34], with updates detailed by Berdanier et al. [35].

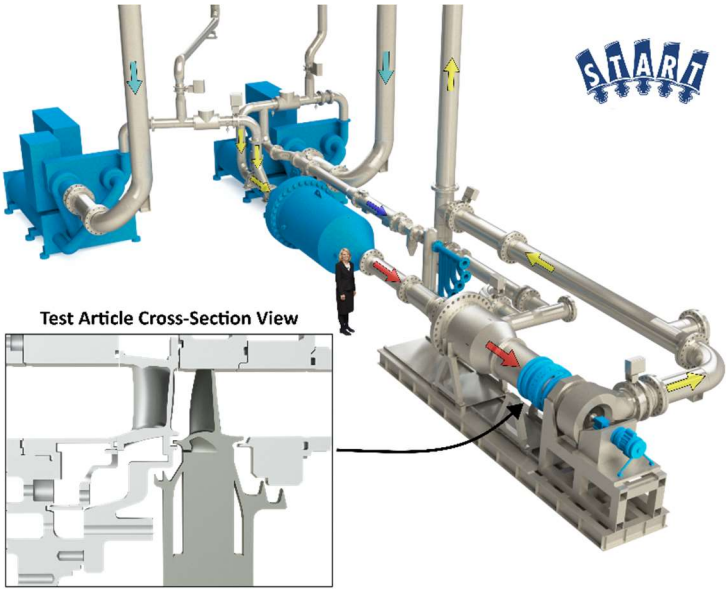

Figure 2.1 START facility with single-stage turbine test section.

The START facility uses two centrifugal compressors to supply up to 10.4 kg/s (25 lbm/s) of air to the turbine. Air exits the compressors at a pressure of up to 480 kPa (70 psia) and a temperature of 395 K (250°F). Most of this air goes into the main gas path, but a portion is split off to use as cooling air. The cooling air is sent through a shell-and-tube heat exchanger to lower the temperature to 273 K (32°F), after which it can be used for three controlled cooling supplies: vane trailing edge (VTE) flow, tangential on-board injection (TOBI) flow through the rotating blades, and purge flow to seal the under-platform cavity.

Air in the main gas path is sent through a natural gas burner, where the temperature can be heated as high as 672 K (750°F). However, a lower temperature was used for this study due to instrumentation requirements. Main gas path temperatures are measured by six thermocouples upstream of the vane at varied circumferential locations. Temperatures of each cooling flow are measured prior to their introduction to the test section. The START rig contains a single stage turbine test section, with one row each of vanes and blades. All blades were previously operated engine hardware, which will be further described in the following sections.

2.3.1 Infrared Thermography Measurements

The START facility utilizes infrared (IR) imaging to capture temperatures on turbine blade surfaces as they rotate at over 10,000 RPM. START's IR system, which was first described by Knisely et al. [36], used a mercury-cadmium-telluride detector in the long-wavelength spectrum. The detector was mounted on top of the START rig, where an optical probe was inserted through the rig casing at different axial positions to capture the images of the blades surface during operation. To view the pressure side and leading edge of a blade, the optical probe was placed in a specially designed, additively manufactured vane upstream of the blades with a viewing window cut from the vane's suction side as seen in Figure 2.2. In addition, a separate measurement port was made to capture the suction side, which is not the focus of this paper. The position of the probe in the vane was such that its placement did not affect the blade being imaged as verified through computational fluid dynamics (CFD).

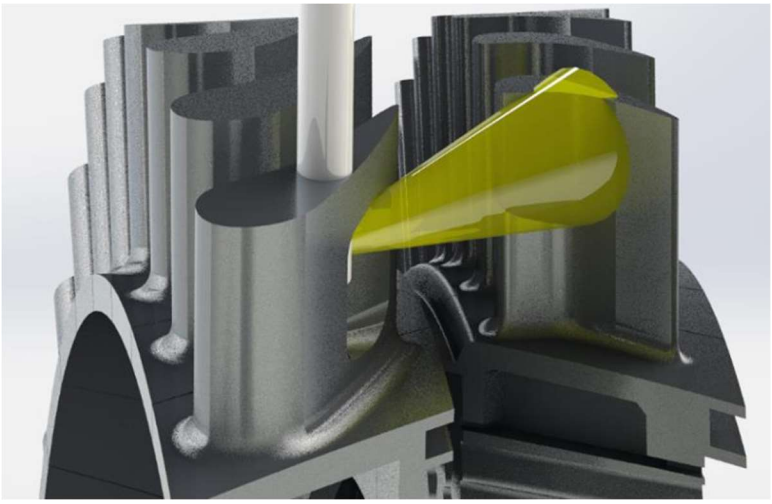

Figure 2.2 IR probe location in the START rig.

The camera angle and radial position were modified throughout testing to take images that encompassed the entire pressure side, suction side, and leading-edge surfaces. Two hundred images were captured at each viewing location and averaged to reduce noise in the final image. A camera

integration time of 2 μs was shown by Knisely et al. [36] to reduce both motion blur and noise during operation, and was therefore used for all images in this study. Phase locking allowed for consistent identification and imaging of specific individual blades as they rotated during testing.

Calibration images were performed to correlate the raw pixel values measured by the camera with detected radiation based on surface temperature. To perform these calibrations, images were taken of a copper plate coated in high emissivity black paint. The temperature of this plate was varied over the entire range of blade surface temperatures expected during testing. The raw pixel values of the camera were then correlated with the expected radiation based on emissivity, surface temperature, and background temperature during the individual calibration. By using this calibration procedure, blade surface temperatures were calculated using only emissivity and rig background temperature during data acquisition. Once completed, the measured temperatures were mapped onto the blade surface through in-house software that was developed by the investigators.

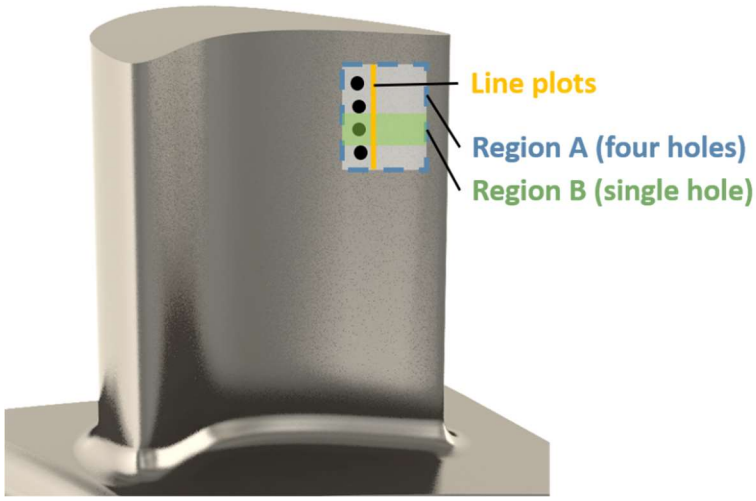

Figure 2.3 Analysis locations of tip trailing edge and mid chord regions.

While images were taken of the entire pressure and suction surfaces, this paper primarily focuses on the pressure side tip trailing edge region, shown in Figure 2.3. Area averaged overall effectiveness was calculated in Region A, where Region A contains a row of four radially-spaced

cooling holes. Additional analysis focused on film cooling trajectories, all of which were calculated for the hole shown in Region B.

Overall cooling effectiveness was used to compare the cooling performance. Cooling effectiveness is a non-dimensional temperature that provides the needed scaling between test turbine and engine blade temperatures provided the relevant non-dimensional parameters are matched to that of the engine. Effectiveness was calculated using Equation 1, using main gas path temperature, blade surface temperature, and cooling air temperature. Blade temperatures were measured using IR thermography, while main gas path and cooling temperatures were measured with thermocouples as described in the facility instrumentation section. Because Reynolds number, Mach number, and Biot number were matched to engine conditions, calculated effectiveness could be used to scale values to true engine temperatures.

$$\phi = \frac{T_{mgp} - T_s}{T_{mgp} - T_c} \tag{2.1}$$

All the data presented in this paper are comparisons of the degradation of the cooling performance using effectiveness values due to environmental impacts relative to a baseline condition.

2.3.2 Uncertainty and Repeatability

Uncertainty in temperature and effectiveness was calculated using methods described by Moffat [37]. The main contributors to bias uncertainty were the calibration, surface emissivity, and background temperatures. For precision uncertainty, the main contributor is the IR detector's pixel value.

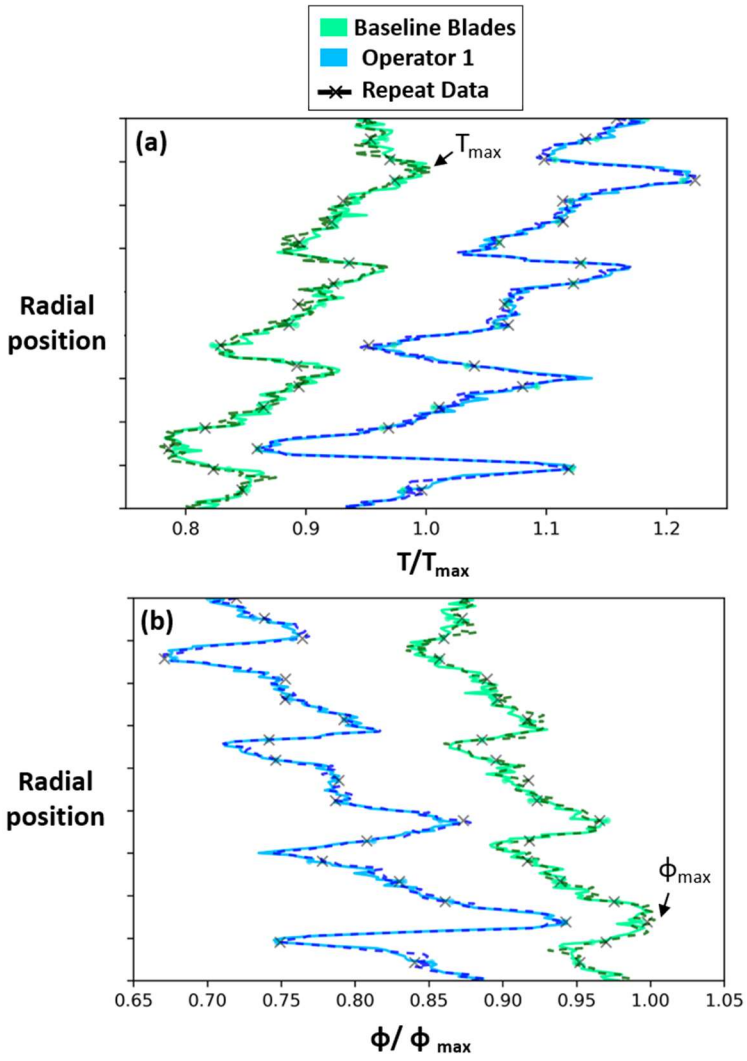

Figure 2.4 (a) Surface temperature and (b) cooling effectiveness plotted behind a row of cooling holes as shown in Figure 2.3. Dotted lines represent the same data taken on a separate test dat. Green lines represent baseline blades and blue lines represent operator 1 blades.

Looking at the bias uncertainty contributions, the calibration uncertainty is dependent on the thermocouples measuring surface and background temperature during the calibration, the emissivity measurement of the calibration surface, and the error introduced by the curve fit correlating the raw pixel values of the camera with measured radiation. The uncertainty of emissivity values for this set of blades was measured and all contributing temperatures were used to calculate background temperature uncertainty. The precision uncertainty within a 95%

confidence interval was calculated for each pixel across the 200 images taken for a given position. For the data reported in this paper, the bias uncertainty of the relative effectiveness values when comparing to a baseline condition, ($\phi - \phi_{bl} / \phi_{bl}$), was calculated to be 0.046 while the precision uncertainty based on the 200 images was 0.037.

To map the images into one composite of the blade surface, consistent and repeatable test conditions in START were required to be replicated over many test days. As an illustration of the repeatability, Figure 2.4(a) and (b) shows the blade surface temperature and overall effectiveness behind the row of cooling holes in Region A. Baseline blades are shown in green and operator 1 blades in blue. The solid and dotted lines for a given color show data taken at the same test condition on different days. The measurements almost entirely overlap, with only slight variations directly behind cooling holes. The typical repeatability from day to day was $\phi/\phi_{max} = 0.003$ while the maximum repeatability differences were 0.015.

2.3.3 Description of Blades Tested

Four sets of blades were tested in this study: one baseline and three operated in engines under different conditions and cycles. All blades had the same geometry and cooling design. Run times were compared to the run time of a set of baseline blades through a non-dimensional Δt shown in Equation 2. The run time of the baseline blades was subtracted from each operator and the entire value was divided by the maximum run time minus the baseline run time.

$$\Delta t = \frac{t - t_{baseline}}{t_{max} - t_{baseline}} \tag{2.2}$$

The environmental and operational impacts for blades of different operators can be seen in Figure 2.5. These sample images were chosen from the pressure side. Baseline blades, shown in

Figure 2.5(a), have a uniform TBC surface, showing no signs of deterioration as would be expected. Figure 2.5(b) shows the surface sample for operator 1 for a benign environment, with a $\Delta t = 1$, having a slight discoloration and deterioration on the surface. The TBC for operator 1, however, is still mostly intact. This level of deterioration is expected for the benign environment that operator 1 blades experienced. Operators 2 and 3 were in a harsh environment, with Δt of 0.75 and 0.4 respectively, and show significant deterioration levels, including TBC spallation revealing bare metal surfaces. As evidenced in these photos, operators 2 and 3 were operated in much harsher environments with high CMAS attack, leading to higher levels of deterioration with shorter run times. All operators showed highest deterioration levels on the pressure side and leading edge.

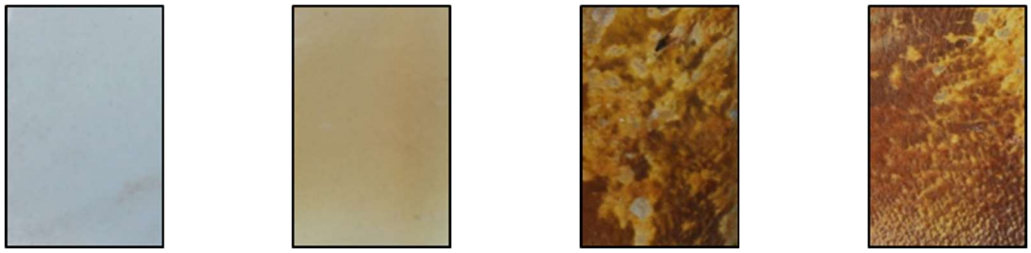

Figure 2.5 Images of blade deterioration for: (a) Baseline blades ($\Delta t = 0$), (b) operator 1 (benign, $\Delta t = 1$), (c) operator 2 (harsh, $\Delta t = 0.75$), and (d) operator 3 (harsh, $\Delta t = 0.4$).

2.4 Blade Flow Variations

Each of the test blades were characterized in terms of their post-operational flow parameter (FP) versus pressure ratio (PR) characteristic. FP encompasses the mass flow weighted by a particular pressure and temperature. Because the turbine test rig sets mass flow for an entire row of blades, the FP is needed to determine the mass flow split for each specific blade. Separate FP measurements were made for the individual internal cooling passages for each blade. To determine

the FP, benchtop flow testing was conducted for each component at a set pressure ratio (PR) and temperature while measuring the mass flow.

The median FP for a particular pressure ratio for each operator is shown in Figure 2.6. The range bars show the minimum and maximum flow within an operator. Each value is normalized by the maximum FP of the baseline blades, which had the highest of the four blade sets tested.

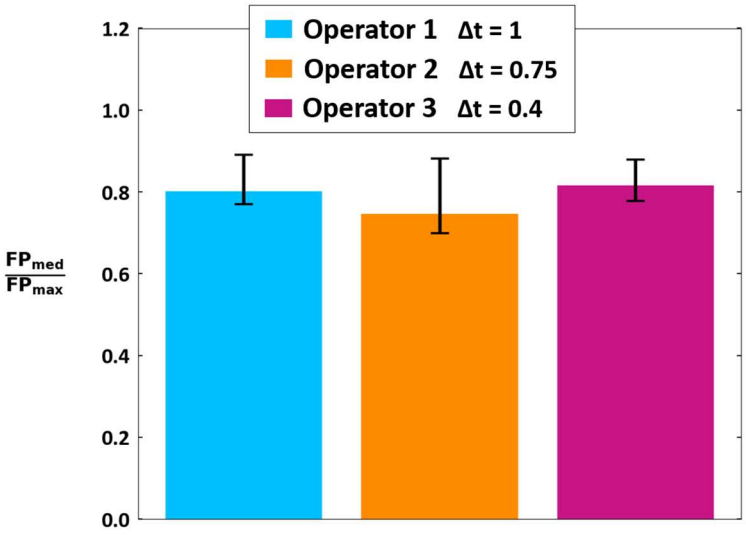

Figure 2.6 Median flow parameter for each operator.

Figure 2.6 shows that operator 3 blades with the lowest run time had the highest flow parameter at 82% of the baseline blade maximum even though these blades were operated in a harsh environment. The median flow blade of operator 1 had a very similar flow parameter to that of operator 3 even though it had the highest run time, illustrating the engine-to-engine variability. Operational and environmental impacts combine to determine degradation of parts, which is illustrated by the similarities between flow parameter for operators 1 in a benign environment with a much higher run time than operator 3 in a harsh environment. Operator 2 blades were the most deteriorated and had the lowest FP, with the minimum flowing blade as low as 70% of the

maximum baseline blade flow. The results for operator 2, also operated in a harsh environment, were because of cooling hole blockages and internal channel deposits.

Operator 2 blades were run in a similar harsh environment as operator 3 but for a longer run time and have nearly twice as much variation in flow parameter. Even though operator 1 blades have the longest run time, they have more similar ranges in flow parameter to operator 3 blades. Harsh environments appear to have caused less consistent deterioration in blades, leading to large variations in flow even within blades from the same engine.

2.5 Blade Durability Impacts from the Environment

As previously described, thermal images of both the pressure and suction sides of the operational blades placed in the rainbow turbine stage were measured. These images were appropriately calibrated and then mapped on to the surface of the blades. It is important to note that temperatures were measured at the surface, which in some cases was intact TBC but where TBC deteriorated represented the metal temperature. Thermal images were appropriately calibrated to account for this variation. Surface temperatures were then put in the form of an overall effectiveness, which is a non-dimensional temperature that uses the upstream main gas path temperature as well as the coolant temperature measured in the cavity supplying the blade root.

The data presented in this section is an augmentation of the overall cooling effectiveness relative to the set of baseline blades at 80% span for the pressure side. The particular blades that were chosen were those with the median cooling flow.

For all cases, the data shown in Figure 2.7 shows significant deterioration of the overall effectiveness levels meaning higher blade temperatures would be expected when operating in the engine. The horizontal black line in Figure 2.7 represents “0,” meaning there is no augmentation relative to the baseline set of blades at that span location. The 0% length occurs at the leading edge

of the blade. As the data in Figure 2.7 approaches zero, it means that there is less degradation since it is closer to the baseline set of blades. Note that exact values are not provided but, rather, this data is used to compare the relative impacts of the environment. The spikes shown in Figure 2.7 occur where there are either cooling holes or image mapping fiducial marks.

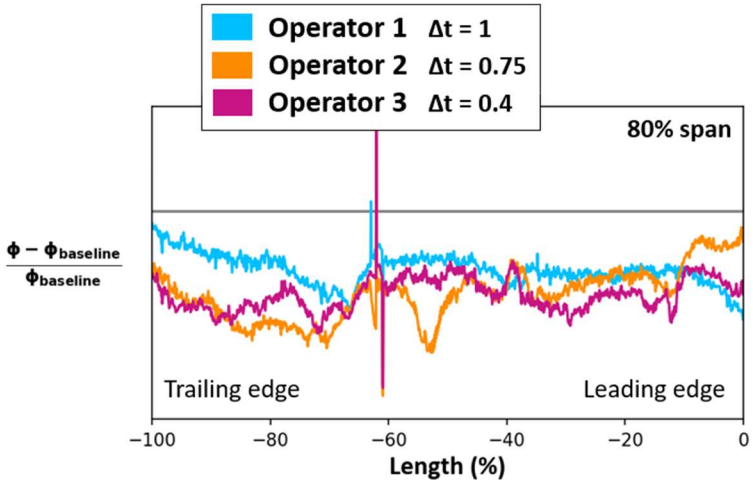

Figure 2.7 Cooling effectiveness around the blade at 80% span. Horizontal line is the "0" value meaning no augmentation relative to the baseline blades.

In reviewing the data presented in Figure 2.7, the reduction of the overall effectiveness is the most similar and the worst for operators 2 and 3 with higher degradation in part because of the operation in harsh environments unlike operator 1. These large decreases in effectiveness occurred on the pressure side at 80% span for all operators where TBC had deteriorated on the engine-run blades.

It is interesting to note that the deterioration relative to the baseline blades indicated the biggest differences between -70% > Length (%) > -100% where all three environmentally-impacted airfoils showed higher values of effectiveness augmentation. The increased augmentation levels indicate that the tip trailing edge was less impacted by environmental factors when compared to the rest of the pressure side surface.

2.5.1 Area-Averaged Cooling Effectiveness

Specific area-averaged cooling effectiveness measurements were made in the region where the blades experienced the highest temperatures. The trailing edge tip region on the pressure side was shown to have the hottest temperatures, which is illustrated in Figure 2.3 in region A. Blades presented in the following figures were the median flow blade within each operator, with error bars showing values for the minimum and maximum flow blade.

Figure 2.8 shows the area-averaged cooling effectiveness for a low and high cooling flow condition for the three operators relative to the baseline set of blades. Note that all values are normalized by the maximum overall effectiveness of baseline blades. The data in Figure 2.8 indicates that all operators showed a reduction in effectiveness from the baseline blades, with the largest reductions in effectiveness seen for the harsh operators 2 and 3.

Even though the blades were operated in a benign environment, in this particular region of the blade for operator 1 with the highest run times, the effectiveness augmentation is still as much as 7% lower than the baseline blade maximum.

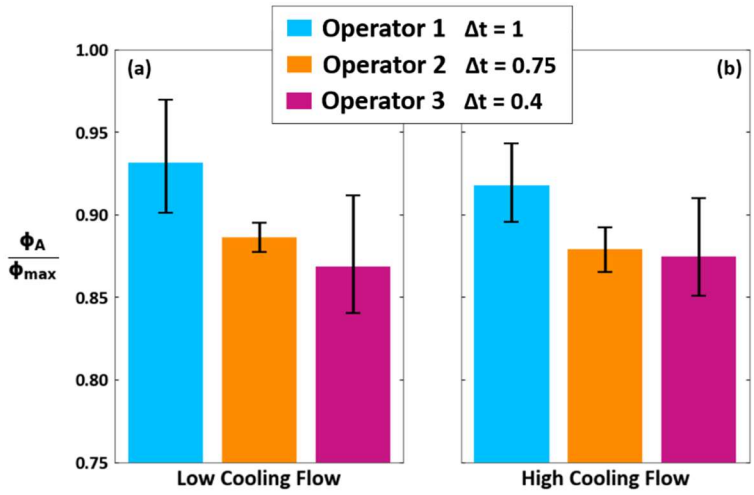

Figure 2.8 Area averaged cooling effectiveness in tip trailing edge region for (a) low and (b) high cooling flow conditions.

For lower coolant flows, operator 3 was lower by 2% relative to operator 2 as shown in Figure 2.8. At a high cooling flow, the effectiveness augmentation varied by less than 1% between operators 2 and 3. This was true even though operator 3 blades had a much lower run time than operator 2 and were expected to have experienced less deterioration.

Figure 2.8 shows that the variability between the blades for operator 3 was higher than the other operators 1 and 2 at both cooling flow conditions. This data indicates that higher variability between blades can occur at shorter operational times in harsh environments.

2.5.2 Film Cooling Trajectories

Applying the methods reported by Knisely et al. [5], specific film cooling trajectories, using the IR images, were evaluated. For the method previously reported by Knisely, the coordinate of the cooling hole start (s') was mathematically defined by using the highest slope in effectiveness along the coolant trajectory. This method was needed since the cooling hole breakouts cannot be detected given the conduction effects. A depiction of the method previously used by Knisely et al. applied to baseline blades is shown in Figure 2.9 [5]. The downstream trajectory of the coolant was then defined using the measured temperatures having the maximum effectiveness.

While this method had previously been used successfully with newly manufactured blades, it was much more challenging for deteriorated blades due to hole blockage and other effects. Trajectories were less clear for deteriorated blades, with the coolant dissipating close to the hole exit or even blowing off the surface. Cooling holes may have been blocked or had very different trajectories due to dirt deposition and TBC deterioration.

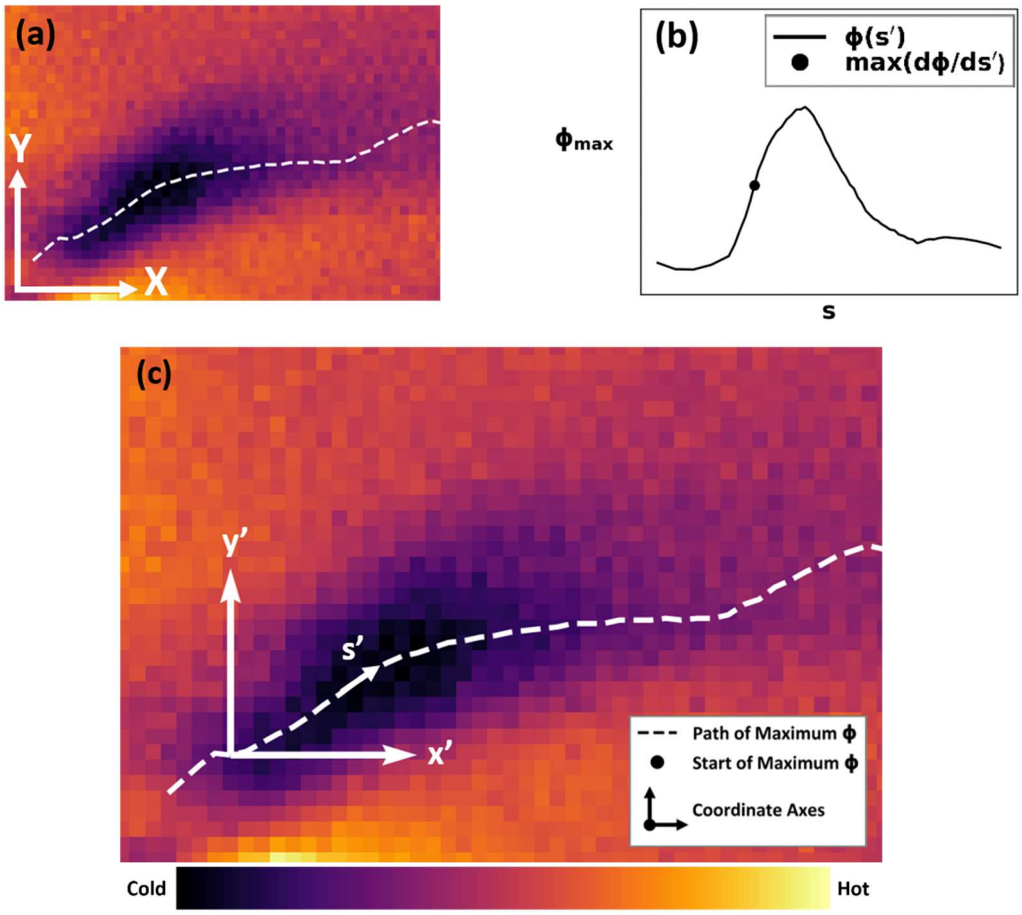

Figure 2.9 Film cooling trajectory method applied to baseline blades including (a) cooling hole with the path of maximum effectiveness applied, (b) illustration of the maximum slope to define s' = 0 at the start of the trace, and (c) cooling trace applied to a cooling hole.

Because coolant trajectories could not be determined due to either no coolant trace or blow off from the surface for the deteriorated blades, the coolant trajectory from the baseline blade was used to define the coordinate system for the cooling holes of engine-run blades. Stated another way, the trajectory of the coolant from the baseline blades was applied to the deteriorated blades. The case for the baseline blade chosen to define the trajectory was that of the mean flow blade to provide comparison of overall effectiveness between operators.

Figure 2.10(a)-(c) shows an illustration of how the coolant trajectory method just described was applied to the deteriorated, engine operated blades. Figure 2.10(a) illustrates the contours from

a single harsh operator cooling hole whereas Figure 2.10(b) illustrates the trajectory defined on the baseline blade for the maximum cooling effectiveness as described by Knisely at al. [5]. Finally, Figure 2.10(c) illustrates the coolant trajectory locations based upon the baseline blades in Figure 2.10(b) applied to the engine operated blade. While the trajectory does not fully represent what is happening in the engine operated blade, it does allow for a consistent method in defining a cooling trace and does provide a comparison of cooling variations due to environmental impacts.

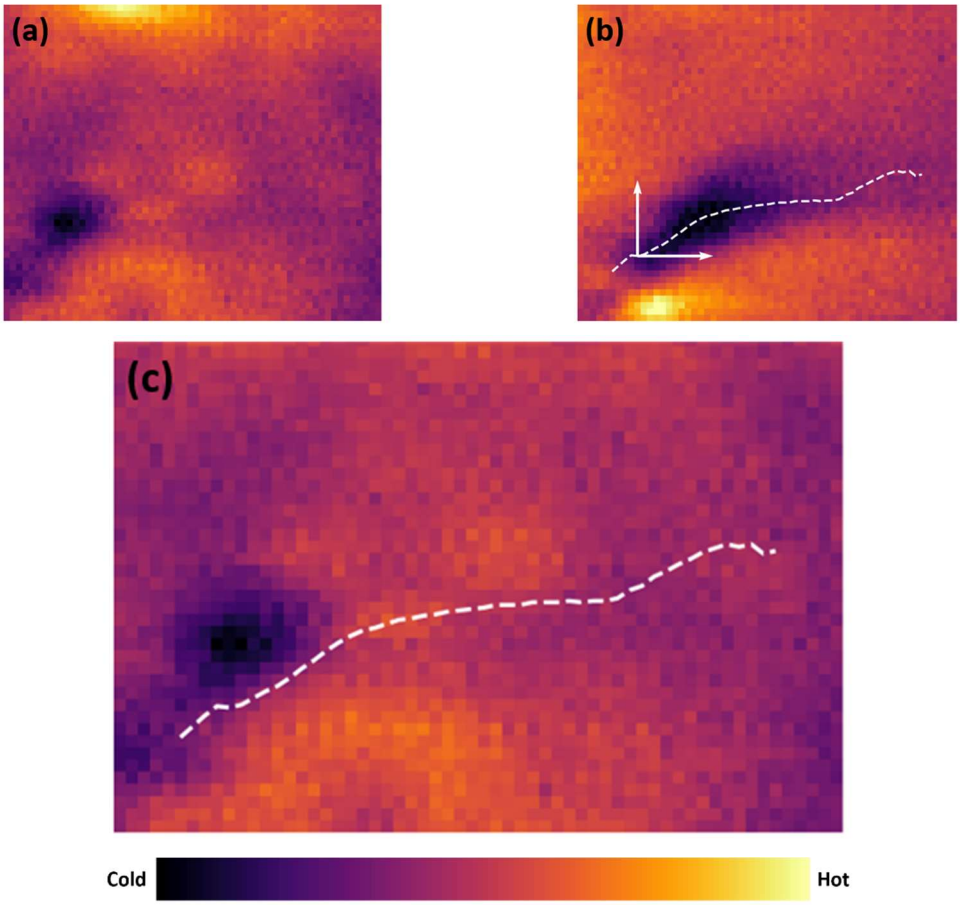

Figure 2.10 (a) Cooling hole on an engine operated blade, (b) cooling hole region with applied trajectory for a baseline blade, and (c) cooling hole on an engine operated blade with trajectory from a baseline blade applied.

Baseline blades, with the shortest run time, were shown to have clearly present trajectories as seen in Figure 2.10(b). There is a region of increased cooling effectiveness starting at the cooling hole, which carries behind the hole as the coolant air reduces blade surface temperature. However, the operator 3 blades run in a harsh environment, as shown in Figure 2.10(c), have a decreased temperature at the cooling hole only. While there is a cold region where coolant air exits the hole, the flow does not stay attached to the surface and therefore there is no region of increased effectiveness behind the hole. Deterioration or blockage of film cooling holes alter the flow and cooling, which was measured most predominantly for operators 2 and 3, both having high CMAS levels due to harsh environments. This lack of cooling leads to higher surface temperatures, which shorten the blade operational life.

The effectiveness value along the film trajectory for the minimum, median, and maximum flow blade of each operator is plotted in Figure 2.11 for Region B in Figure 2.3. The case chosen to evaluate was for a high coolant flow. The gray shaded region in Figure 2.11 notes the range of the blade flows over all four operators, and the dashed lines show the median flow blade of each operator. Data for all blades within each operator can be seen in Figure 2.12. All values are normalized by the maximum overall effectiveness of a single baseline blade.

Figure 2.11 shows that the baseline blades have a high effectiveness for six hole diameters downstream of the cooling hole shown in this figure. However, the effectiveness values decrease closer to the hole for engine-operated blades. While the median flow blade of operator 1 had a slightly higher effectiveness than operators 2 and 3, there was still a significant reduction from the baseline blades. The harsh environment blades of operators 2 and 3 had similarly low effectiveness, even though operator 2 blades had a longer engine run time.

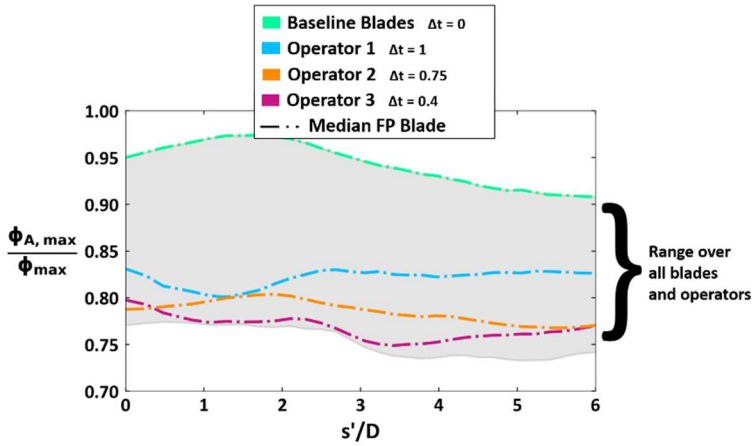

Figure 2.11 Effectiveness along cooling trajectory as a function of s'/D behind a cooling hole.

To see further details relative to Figure 2.11 for each blade set, the maximum effectiveness along the cooling trajectory for all blades within each operator is shown in Figure 2.12(a)-(d). The FP values were defined for the entire blade and are not specific to region B in Figure 2.3. Note that the effectiveness for each blade set was normalized by the maximum of the baseline blades. The minimum, median, and maximum flow blades are shown in dashed, dashed-dotted, and solid lines, respectively.

The baseline data in Figure 2.12(a) shows less variation in the maximum cooling effectiveness for the set of baseline blades compared to those for operators 1-3. Each of the data sets for the operators had its own characteristic decay shape. The blade temperatures for operator 1 indicated nearly a flat profile for all the cases as shown in Figure 2.12(b). Since all the holes for the different flow cases resulted in the same blade temperature profile, it implies that the film-cooling in this region is not dominating or that for every case the trajectory for the baseline blades does not capture the decay.

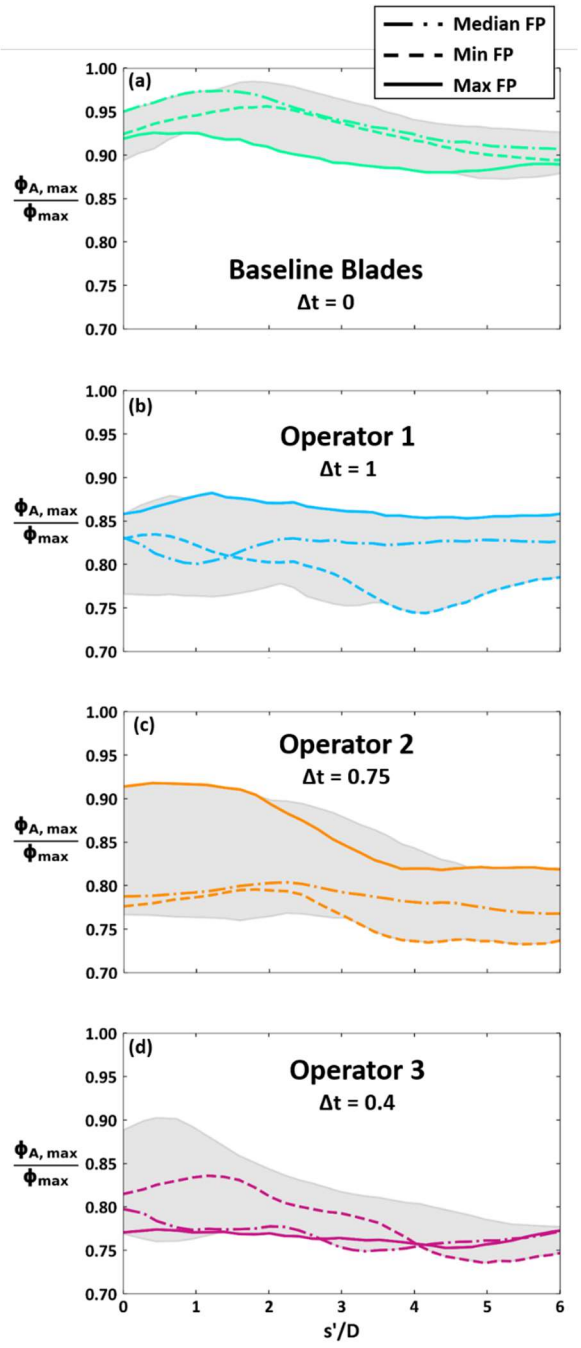

Figure 2.12 Film trace overall effectiveness for (a) baseline, (b) operator 1, (c) operator 2, and (d) operator 3 blades normalized with a singular baseline blade.

Operator 2 and 3 both have a large range of overall effectiveness at the cooling hole as shown in Figure 2.12(c)-(d). The data also shows that the coolant significantly decays after only

one- or two-hole diameters. Further from the cooling hole, the flow appears to be detached and effectiveness is low for all blades operated in harsh environments. However, the maximum effectiveness directly at or behind the hole is higher for some of the harsh operator blades than for the benign operator blades, even though it does decrease significantly further from the hole.

Although blades with higher flow parameter would be expected to have higher cooling effectiveness, this was not the case for many of the blades shown in Figure 2.12(a)-(d). The maximum flow blade did have the highest cooling effectiveness for operators 1 and 2, but not for the baseline blades or operator 3. For the baseline blades, the blade with the maximum flow parameter had nearly the lowest cooling effectiveness behind the cooling hole. Additionally, the lowest flowing blade for three of the four blade sets had a higher cooling effectiveness than the median flow blade at some point downstream of the cooling hole.

Because the flow parameter measurements were for the entire blade, they do not necessarily correlate with the amount of flow through this individual cooling hole. As blades deteriorated during operation, cooling holes were more likely to become blocked and variations in flow between individual cooling holes are expected. Even in newly manufactured blades, Knisely et al. [5] showed that flow through smaller regions did not necessarily correlate with flow through the entire blade. Total flow parameter was therefore not necessarily indicative of flow through a cooling hole, and even blades with the same amount of flow could experience different paths of cooling flow on the blade surface, thus changing the region's effectiveness.

2.5.3 Estimates of Blade Lifing

Scaling the data from the measured blade surface temperatures using overall cooling effectiveness, ϕ, provides the ability to use the data to estimate blade surface temperatures in an operating engine. It is noted that the operating conditions of START are at much lower pressures

and temperatures relative to the engine, but given the relevant non-dimensional numbers are matched to that of the engine (Re, Ma, and Bi), the scaling is possible. To illustrate the impacts of the environment on the blade temperatures, a non-proprietary set of conditions were chosen to be those from the NASA E^3 [27] engine. These values are shown in Table 2.1. For this analysis, the minimum effectiveness values (highest surface temperatures) determined from the infrared image measured on the pressure side of each blade was used for the scaling to the NASA E^3 engine conditions.

Table 2.1 NASA E^3 Engine Temperatures

Quantity	NASA E^3 Value
Cooling Air Temperature, T_c	628°C (1162°F)
Main Gas Path Temperature, T_∞	1396°C (2545°F)

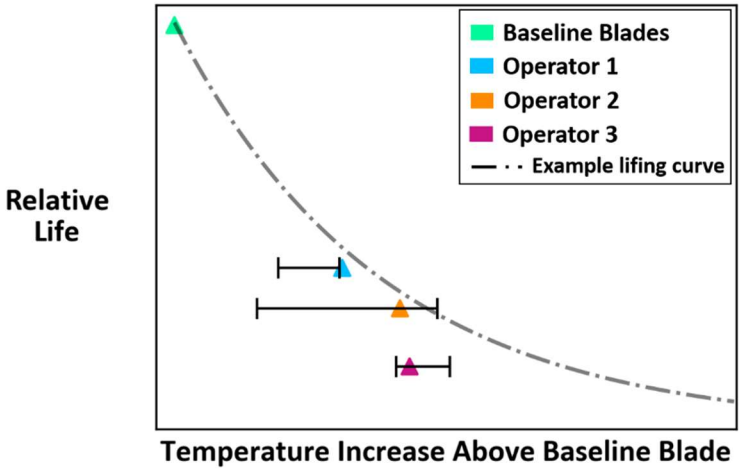

Figure 2.13 Blade life curve with baseline and operator 1-3 blades.

Increases in scaled temperatures at E^3 engine conditions can be seen plotted against the relative blade life in Figure 2.13 along with an example lifing curve [5]. The bars in Figure 2.13 represent the ranges in the minimum effectiveness that occurred within a particular blade set on the pressure side. The median point for operator 1 blades fell along the lifing curve, showing that

current predictions can estimate blade life for benign environments as shown in Figure 2.5. However, blades operated in harsh environments fell below the lifing curve, particularly operator 3 blades. Operator 3 blades had a much larger surface temperature increase than expected for the run time of these blades. These were much worse than operator 2 blades, which had a similar increase in surface temperature but a much longer run time. This decrease in life resulted from the high levels of deterioration that occurred in the heavy CMAS environment, causing decreased cooling performance and shortened life for these blades.

2.6 Conclusions

This study determined the effects of engine operation across varied environments on flow and cooling effectiveness. Three operators, all with different run times and environments, were compared with a set of baseline blades. The environments included operator 1 from a benign environment and operators 2 and 3 from harsh environments. The changes in flow and cooling effectiveness due to deterioration in both benign and harsh environments were then compared through multiple approaches.

Flow parameters were measured at a given pressure ratio for all blades in this study. The median flow parameter was highest for baseline blades, with reductions in FP of almost 30% for blades operated in harsh environments. In addition to variations between operators, large flow parameter variations within the same operators indicated that blades did not deteriorate uniformly even when operated at the same conditions.

Overall effectiveness levels were analyzed along the pressure side near the blade tip. Harsh operators showed decreases in effectiveness being impacted at the 80% span which coincided with regions where the TBC was absent. When looking at the tip trailing edge region, area averaged

effectiveness was very similar for both harsh operators at both high and low TOBI flow rates, while being much lower than either benign or baseline blades.

Film cooling trajectories behind a specific cooling hole across all operators were compared between the blades. For the baseline blade, clear trajectories of the film were identified with the location applied to all blades in this study. This showed consistently high cooling effectiveness downstream of cooling holes for baseline blades, while effectiveness dissipated close to the hole for deteriorated blades. Effectiveness showed large variations immediately downstream of cooling holes in engine run operators, but low effectiveness values after one- or two-hole diameters for all deteriorated blades.

Effectiveness values in this study were used to predict blade surface temperatures scaled to the NASA E^3 engine. This showed large increases in surface temperature at true engine conditions, leading to significant reduction in expected life when compared to published lifing models.

This study provides a new understanding of how blade flow and overall blade temperatures vary based on part deterioration levels and impacts of different environmental effects. The results presented give a good indication of the part-to-part variations in deterioration between operators and even within the same operator. This knowledge will help to improve blade lifing models for a range of run times and operational environments.

Chapter 3

Geometric and Flow Characterization of Additively Manufactured Turbine Blades with Drilled Film Cooling Holes

Abstract

As designers investigate new cooling technologies to advance future gas turbine engines, manufacturing methods that are fast and accurate are needed. Additive manufacturing facilitates the rapid prototyping of parts at a cost lower than conventional casting, but is challenged in accurately reproducing small features such as turbulators, pin fins and film cooling holes. This study explores the potential application of additive manufacturing and advanced hole drill methods as tools to investigate cooling technologies for future turbine blade designs. Data from computed tomography scans are used to non-destructively evaluate each of the cooling features in the blade. The resulting flow performance of these parts is further related to the manufacturing through benchtop flow testing. Results show that while flow through the entire blade is consistent throughout a full wheel of the additively manufactured cooled blades, flow through smaller regions show larger variations. Shaped film cooling holes manufactured using a high-speed electrical discharge machining method are within tolerance in the metering section but do not expand at the specified angle in the diffuser even though design tolerances are met. In contrast to high-speed EDM, conventional EDM holes are undersized throughout the length of the hole. The roughness results show high levels on thin walls, particularly at the trailing edge as well as on downskin surfaces. Internal surface roughness is higher than external roughness at most locations on the blade. The results of this study confirm that additive manufacturing along with advanced hole drilling techniques offer faster development of blade cooling designs.

3.1 Introduction

The manufacturing of turbine airfoils using traditional casting approaches is an expensive and time-consuming process that is not conducive to rapid technology iterations. As turbine inlet temperatures increase to meet ambitious efficiency goals, new cooling technologies are essential to enable the next generation of gas turbine engines. Additionally, quantifying the durability of components with aggressive designs is needed to ensure sufficient life for these parts. By using advanced manufacturing processes, new turbine airfoil designs can be investigated faster and at lower costs while still representing the performance of real hardware.

The Penn State Steady Thermal Aero Research Turbine (START) Laboratory was built to test turbine components at engine-scale with relevant conditions to measure performance and life [34]. The START Lab has developed the National Experimental Turbine (NExT), a single-stage, fully-cooled test turbine to research true-scale engine hardware, in partnership with four gas turbine manufacturers and supported through the U.S. Department of Energy-National Energy Technology Laboratory [38]. NExT allows engine manufacturers to evaluate next-generation technologies to drive forward the development of future gas turbine engines targeting increased efficiency and durability.

To support accelerated manufacturing timelines for the NExT program, a variety of advanced manufacturing methods were used to produce airfoil components. The initial set of NExT blades and vanes was manufactured using laser powder bed fusion (LPBF) additive manufacturing (AM) to circumvent long lead times and high costs associated with casting development parts. This initial set of blades also offered the opportunity to study impacts of the additive process on turbine performance. While AM has only recently been used in stationary main gas path parts [39–41], this metal printing technology has scarcely been publicly reported for rotating turbine blades given the thermal stresses that blades experience [42–44]. Because START operates at temperatures and

pressures lower than that of today's turbines, AM blades are viable in the research turbine allowing for faster development turnaround times.

Additive manufacturing still faces challenges, however, in making small features relevant to aircraft engine sizes such as turbulators, pin fins, and film cooling holes [45]. For this reason, industry-standard hole drilling methods like EDM were used for the NExT airfoils. To investigate the most advanced EDM technologies, two different methods were used for NExT to evaluate the differences.

The combination of manufacturing methods, AM and EDM, supports accelerated development of components without sacrificing the quality of film cooling features for durability measurements. This study highlights the manufacturing advantages and challenges of the application of AM for airfoil cooling technologies so that future applications of AM can effectively utilize its benefits while anticipating the challenges. The present study focuses on the geometric variations and their associated changes to the flow throughout the parts through static tests. This study is the first of its kind to characterize the feasibility of using AM components to research the cooling performance of cutting-edge blade cooling technologies in a turbine stage. Additionally, this study presents the first additively manufactured cooled blades spun in a university laboratory.

3.2 Literature Review

While there is scarce public literature available on the manufacturing variations of final components for cast turbine hardware, Bunker [4] published a study that discussed manufacturing tolerances and typical variations of features in turbine blades and vanes. This study looked at over 30 features and quantified typical sizes and tolerances, as well as their effects on cooling. High external surface roughness levels led to increased external heat transfer coefficients and made parts more likely to become even rougher during service due to degradation. For film cooling holes, the

exit shape was found to have the largest variation due to difficulties accurately manufacturing expansion angles. This variation caused film effectiveness to increase by up to 16% or decrease by up to 13% depending on the change in shape. Crossover holes used to meter internal cooling flow showed diametral variations of 10% resulting in a one-to-one (10%) variation of internal heat transfer coefficient. Manufacturing variations in other internal features such as turbulators and pin fin arrays, particularly the height and angle relative to the flow for turbulators and pin spacing for pin fin arrays, were shown by Bunker to have impacts on internal heat transfer and pressure drops. Characterizing variations in these types of features for the additively manufactured NExT blades is the focus of the current paper.

Variations in flow and cooling effectiveness for cast turbine blades with EDM holes were previously published by both Knisely et al. [5] and McCormack et al. [46]. Knisely et al. showed that for a set of development-grade cast blades, flow through the entire blade varied by up to 20% of the mean value of the full blade set. Additionally, flow through individual film cooling holes varied by up to 55% of the individual mean value. However, the magnitude and trends of the flow through single holes were not necessarily indicative of the flow through the rest of the blade. For example, one blade which underflowed by about 20% contained a single cooling hole which overflowed by almost 20%. These flow variations led to disparities in peak cooling effectiveness of up to 15% behind the cooling holes. McCormack et al. found that variations in flow and cooling effectiveness were even larger for engine-run parts that had experienced high levels of environmental deterioration than they were for new development blades studied by Knisely et al. Flow through deteriorated blades was as much as 30% lower than the baseline blade values, causing a decrease in peak cooling effectiveness of almost 20% behind a row of cooling holes.

The additive manufacturing process can lead to different types of manufacturing variations as compared to cast components. One such variation is the high roughness on additively manufactured surfaces relative to cast surfaces. The surface roughness inherent to additive

manufacturing is dependent on many factors including laser power, laser scanning speed, hatch distance, laser scanning strategy, wall thickness, and contour settings [47]. Build direction also has significant effects on roughness, with unsupported downward facing surfaces having much higher roughness than upward facing or vertical surfaces [48,49]. Moreover, thin additively manufactured features suffer from increased conduction resistance resulting in significant heat accumulation [50,51], leading to larger melt pools [52]. These large melt pools allow more groupings of particulates to bond to the surface, resulting in high roughness on thin walls [53]. The increased roughness levels resulting from AM lead to similar heat transfer and pressure drop augmentations as that of engineered ribs used in cast components [47,54]. While external surfaces can undergo post-machining smoothing processes, these processes are challenging or non-existent for internal surfaces of aviation-scale airfoils. These internal cooling features are small and could be damaged or removed by relevant post-processing methods.

Additively manufactured internal cooling features in flat coupons, such as pin fins arrays and ribs, have been studied in recent years. Kirsch and Thole [55] found that pin fin cross sections were not necessarily circular with the downskin (unsupported) surface having exceptionally high roughness levels and even loose particles attached around the pin base. Another study by Corbett et al. [56] found that roughness was significantly higher on the channel walls than on the pins themselves, which was attributed to test coupon walls that were thinner than the pin thickness. Both studies showed higher heat transfer than similar designs of traditionally manufactured pins. Further work focused on additively manufactured turbulators by Krille et al. showed up to 60% higher heat transfer and double the pressure loss compared to traditionally manufactured turbulators with the same design [57]. Additionally, large roughness elements of the size resulting from additive manufacturing can cause augmentations in heat transfer that are comparable to turbulators of a similar height [47].

While there have been attempts to print small features such as film cooling holes, results have shown additively manufactured film cooling holes experience blockages and deformations [58,59]. Previous research has explored ways in which film cooling hole shapes vary due to manufacturing effects when using the conventional EDM process [23,60–65]. A variety of EDM methods can be used, with the entire hole being drilled in one step or the meter and diffuser machined separately [61,66]. To study how these drill processes affect performance of film cooling holes, Haydt et al. [62,63] studied conventional manufacturing variations in 7-7-7 holes [65]. Their studies showed significant impacts on film-cooling benefits resulting from manufacturing defects.

For conventional EDM hole manufacturing, a controlled spark is used to create a cooling hole matching the shape of the electrode itself. In addition to conventional EDM hole drill methods, a relatively new category of high-speed EDM has been used in recent years. While conventional EDM uses electrodes that match the shape of the features, high-speed EDM uses a single cylindrical electrode with different drilling motions to complete complex shapes [67]. The high-speed EDM process differs from the conventional EDM method in that the electrode used is not made to match the cooling hole shape and, instead, is moved using a multi-axes EDM machine. For a high-speed EDM process, the cylindrical electrode is used in three steps: first, a small entry hole is drilled to the depth of the diffuser; second, the electrode is moved radially outward to create the diffuser shape; third, the metering section is drilled to complete the hole.

In contrast with prior literature, this paper provides a unique view of feature variations due to additive manufacturing and film-cooling hole drilling in true-scale turbine components. The purpose of this study is to examine the manufacturing methods and variations in a set of NExT turbine blades with a particular focus on specified tolerances. Additively manufactured blades created using two different hole drill methods are analyzed and compared to their design intent. Blade features such as cooling holes, turbulators, pin fins, and crossover holes are characterized and compared to their design intent and compared in terms of flow measurements. This analysis

allows for comparison between as-built parts and design intent for both additively manufactured cooling features as well as film cooling holes manufactured using conventional and high-speed EDM techniques. Ultimately, the results impact the understanding of manufacturing methods for advanced engine-relevant cooling designs.

3.3 NExT Geometry and Manufacturing

The turbine stage with cooled blades in this paper used the NExT testbed [38], which was designed through a collaborative effort between academia, industry, and government. The NExT airfoils use modern cooling features such as serpentine channels, rib turbulators, film cooling holes, and pin fin arrays. The turbine stage was specifically designed for integration into Penn State's START facility, through which NExT technology demonstrations provide direct utility to industry partners. START is able to produce engine-relevant conditions as described by Barringer et al. [34] with true-scale hardware. For the START facility, a set of NExT vanes and blades were additively manufactured with film cooling holes drilled using both conventional and high-speed EDM methods after printing. Although vanes and blades for the initial NExT build were both additively manufactured, this study specifically focuses on the cooled blades. For the additive manufacturing process, Inconel 718 was used along with best practices developed after several trials resulting in the build orientation of the blade shown in Figure 3.1. Figure 3.1 shows the suction side of the blade.

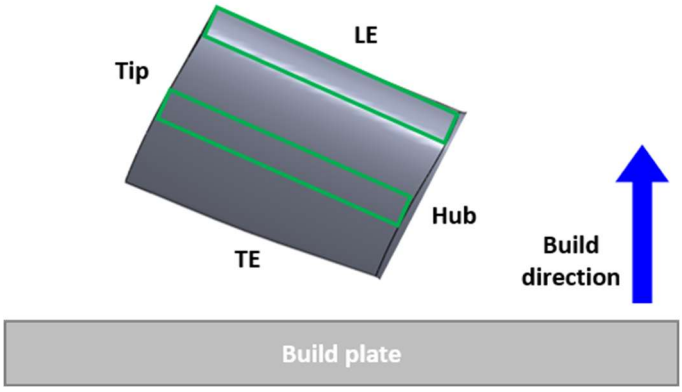

Figure 3.1 NExT blade build orientation for additive manufacturing showing the suction side. Green boxes represent the location of turbulators on the internal wall.

A representation of the NExT cross-section of the blade, as first presented by Thole et al. [38], is shown in Figure 3.2. Various internal cooling channels with ribbed turbulators, shown as red lines along the walls, run through the blade and feed cooling holes on the surface. Crossover hole features (A, B) through blade internal walls allow flow to pass between two channels to meter the flow. Turbulators were investigated on the suction side wall in two locations: one near the leading edge at (C) and one near the trailing edge (D). Film cooling hole rows are illustrated in Figure 3.2 with blue arrows. The present study focuses on film rows labelled (E, F, G, H). Finally, the trailing edge (TE) of the blade contains a pin fin array (I), which was also evaluated relative to the design intent.

The designs for the film cooling holes studied in this paper are described in Table 3.1 as compared to typical 7-7-7 holes [65]. All shaped holes studied were designed with 7° expansion angles as shown in Figure 3.3(a) and Figure 3.3(b). The metering diameter for each was the same at 0.46 mm. The injection angle and hole length were equal for holes in rows G and H, however, row F on the suction side (SS) had a higher injection angle and longer metering section.

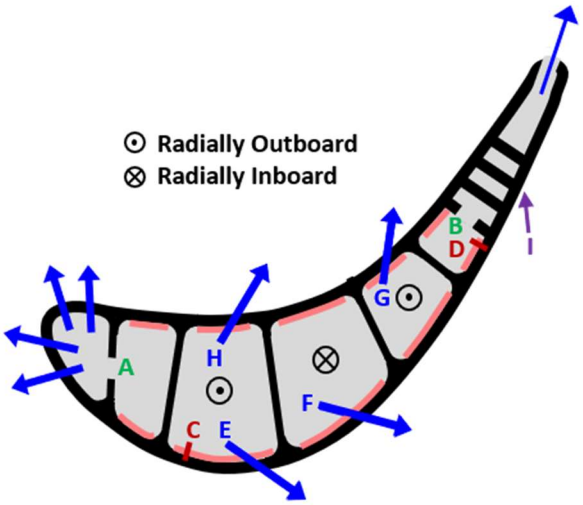

Figure 3.2 NExT blade schematic with relevant cooling features labeled. Green labels (A, B) represent crossover holes; red labels (C, D) represent turbulators; blue labels (E, F, G, H) represent cooling holes; and purple labels (I) represent pin fins, which were all evaluated in this study.

Table 3.1 Cooling Hole Designs

	Standard 7-7-7 hole [65]	Row F	Row G	Row H
Lateral expansion angle, β_{lat}	7°	7°	7°	7°
Forward expansion angle, β_{fwd}	7°	7°	7°	7°
Injection angle, α	30°	35°	30°	30°
L_m/D	2.5	2.5	1.8	1.8
L/D	6.0	6.0	5.3	5.3
D	–	0.46 mm	0.46 mm	0.46 mm

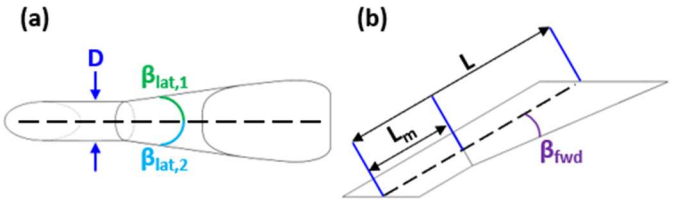

Figure 3.3 (a) Top view and (b) side view of a shaped film cooling hole.

Details on how both hole drill methods were applied for NExT hardware are presented in Table 3.2. For the film cooling holes labeled row H in Figure 3.2, conventional EDM method was used. The conventional method used a copper electrode manufactured to match the combined shape of the intended hole and the diffuser. However, the electrode was slightly undersized to account for anticipated overburn during the EDM process. This conventional EDM method used for the NExT hardware where the hole and diffuser are manufactured concurrently is similar to EDM methods used on many turbine components [61]. For holes with direct line of sight, including rows F and G, the high-speed EDM method made use of a vendor's developments for cooling hole manufacturing with increased speed [67].

The tolerances governing manufacturing of all cooling holes included the diameter in the metering section and a profile tolerance of the shaped diffuser. The location of these measurements when looking into a film cooling hole can be visualized in Figure 3.4. The solid lines show the design intent shape, while the dashed lines show the maximum allowed tolerance variation. The metering hole diameter, shown in green in Figure 3.4, was deemed acceptable within ± 0.076 mm. The 0.15 mm profile tolerance defines the range about the designed surface geometry in which the manufactured shape must fall. Profile tolerances of 0.15 mm represent a standard manufacturing tolerance for drilled holes, making this study directly applicable to understanding effects of hole manufacturing of true engine hardware. Because the manufacturing method was not explicitly prescribed for each hole on the blade, the tolerance specifications apply universally to all holes on the airfoil. However, the holes drilled using conventional one-step shaped diffuser electrodes were subject to additional quality control from the manufacturing of the shaped electrode itself. Specifically, the shaped electrode diffuser angle was specified by a tolerance band within 0.5° of design intent.

Regardless of manufacturing method, the overall shape of these cooling holes can vary significantly but still remain in tolerance, as seen in Figure 3.5. Figure 3.5 shows an illustration of

the two worst-case scenarios for metering hole size. The dotted lines on these figures show the tolerance for the holes, and blue lines indicate potential cooling hole shapes governed by the profile tolerance. Because the metering section and diffuser were not manufactured in the same step for the high-speed EDM holes (although they are performed sequentially on the same machine), the size and shape of the two sections could vary independently. These variations can impact the flow through the holes and subsequently the cooling effectiveness behind the holes. Within the 0.15 mm profile tolerance, diffuser angles can vary by up to 4° depending on the cooling hole shape. Lateral expansion angles between 2.9° and 11.0° would still meet tolerance specifications at the hole exit profile for hole rows F, G, and H. Forward expansion angle has an additional dependence on the cooling hole injection angle, with an acceptable range of 4.1° to 10.4° for rows G and H or 3.9° to 10.5° for row F.

Table 3.2 Description of Hole Drill Methods and Design Tolerances

	High-Speed EDM	Conventional EDM
Hole Rows	SS, LE, Tip, Platform, all but one on PS	One on PS
Hole Rows Evaluated (Figure 3.2)	E, F, G	H
Hole Design	Cylindrical, Shaped	Shaped
Metering diameter tolerance	± 0.076 mm	± 0.076 mm
Profile tolerance	0.15 mm	0.15 mm

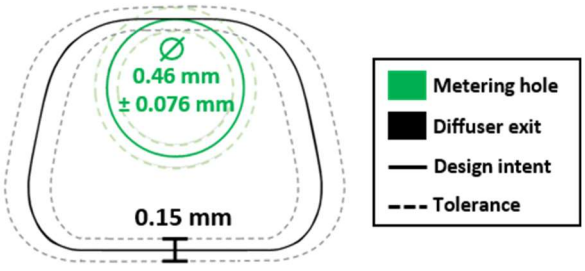

Figure 3.4 Film cooling hole tolerances for the metering section and diffuser exit profile looking directly into the hole.

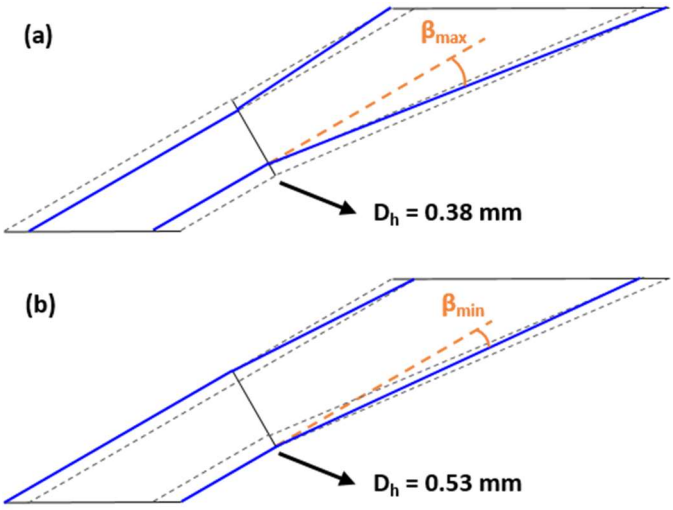

Figure 3.5 Side view of tolerances for shaped cooling holes, showing variations in acceptable cooling hole shapes for (a) the minimum possible meter diameter and (b) the maximum possible meter diameter.

3.4 Flow Measurements

The flow performance of each blade in the turbine wheel was characterized by evaluating the flow parameter (FP) over a range of pressure ratios (PR) using a static benchtop test rig. The blade root was fixed in a custom-built gasket to seal the inlet. The pressure entering the blade was set using a mass flow controller, which also measured mass flow rate and temperature. The flow performance was characterized in two ways for this study: the full blade flowing or a partial blade flowing. During the testing with the partial blade, sections of the blade were specifically blocked using foil tape to evaluate individual holes or rows of holes. Measurements were taken both while increasing and decreasing pressures to monitor hysteresis, both of which are shown in Figure 3.6. The measurements followed a consistent trend both when increasing and decreasing pressure. A propagation of uncertainty analysis was conducted for each measurement using the guidelines established by Figliola and Beasley [68]. The bias uncertainty of normalized flow parameter FP/FP_{ref} was 0.0087, while the bias uncertainty in PR at design point was 0.0061.

Figure 3.6 shows the flow parameter normalized by the flow parameter at the design pressure ratio (FP_d) for the full blade as a function of pressure ratio. The three blades shown as solid points were selected from the set based on the data indicating these had the minimum, median, and maximum flow parameter at the design pressure ratio. The gray range represents the entire range of flow parameters for all blades in the stage. At the design pressure ratio, the flow parameter varied by less than 10% between the minimum and maximum flow blades. All blades in the set fell within the acceptability range for FP as defined at the design pressure ratio.

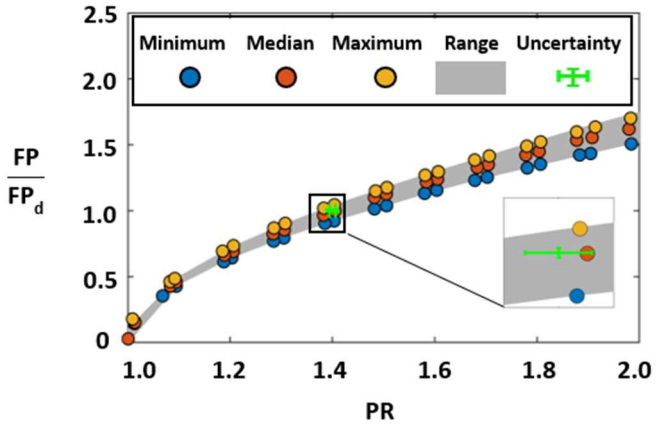

Figure 3.6 Flow parameter normalized by the design intent flow parameter at a PR=1.4 over a full range of pressure ratios for the entire set of blades (gray shaded region) highlighting the minimum, median, and maximum flowing blades.

For the partial flow tests, measurements were collected from three selected blade locations using the minimum, median and maximum blades, based on their full blade flows as highlighted in Figure 3.6. The specific locations were: the pressure side (PS) and tip (G, H from Figure 3.1 and tip holes), the suction side (SS; E, F), the leading edge (LE; four rows of holes making up the showerhead), and the trailing edge (TE; pressure-side cutback slots). The results of the partial-blade flow tests are given in Figure 3.7 where the measured flow parameter for each section is given as the percent difference from the design flow parameter for each section.

Results in Figure 3.7 also show the acceptability range as defined for the full blade, and dashed lines show this same relative range applied to the partial flow measurements. Because flow acceptance criterion is only explicitly defined for the full blade, it is possible for the full blade flow to meet blueprint specifications while particular blade regions do not. For the selected blades, all three overflowed in the PS, SS, and in the tip region; the TE region underflowed; and the LE flow parameter varied with primarily underflowing behaviors. The trailing edge region had the most consistent flow between blades, showing flow variations less than 2% between blades. The three other regions, as shown in Figure 3.7, had variations in flow of approximately 16% between the highest and lowest flowing blade in each section. While the maximum flow blade had the highest flow parameter in three of the four regions, the median flow and minimum flow blade were less consistent in their trends, with the minimum flow blade only flowing the least for two of the four regions. Causes of the significant variations in flow performance were further evaluated in subsequent sections by determining areas of maximum deviation of cooling features from design intent.

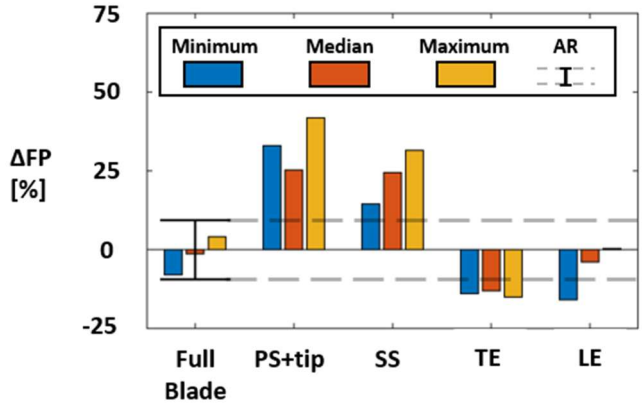

Figure 3.7 Partial blade flow for three selected blades, shown as percent difference from design flow parameter. Full blade acceptability range (AR) is shown in black bars on the full blade, with dashed lines extrapolating the same range for partial flow data.

3.5 Film Cooling Hole Deviations

A detailed analysis of internal and external geometries was used to explain the flow variations identified in Figure 3.7. Specifically, data from computed tomography (CT) scanning for the minimum, median, and maximum flow blades were used to compare as-built parts to the design intent. CT scanning provided high resolution, nondestructive measurements of internal and external surfaces. A voxel size of 40 μm was used for the CT, which resolved features to within 4 μm in post-processing [69]. The blade surface was determined using commercial software and additional analyses were performed using in-house processing codes. The CT data were also used to quantify surface roughness values.

The analyses of the film cooling holes focused on the three rows of holes described in Table 3.1 with two on the pressure side (G, H) and one on the suction side (F). As described in Table 3.2, the row of holes (F) on the suction side and one row of holes (G) on the pressure side were both drilled using high-speed EDM, whereas the other pressure side row (H) was drilled using a conventional EDM method. To measure the cross-sectional area and perimeter of these film cooling holes, 60 slices perpendicular to the hole axis were analyzed across the hole length. Using an in-house processing code [70], the cross-sectional area and perimeter were quantified and then used to calculate hydraulic diameter (D_h).

To ensure that the number of measured holes would statistically represent the cooling hole diameter on a given blade, a study was performed using all holes in one row on the suction side for the blade with median flow. The holes were randomly selected in groups with different populations, and a sample size was considered sufficient when the precision uncertainty for all groups of that size was smaller than the bias uncertainty of the CT scans (i.e., half the voxel size, 20 μm). The highest precision uncertainty for groups of three holes using this approach was calculated to be 16

μm, therefore the hydraulic diameter of three holes in each row was measured on each blade for analysis in this study.

The mean diameters of the metering section normalized by the design diameter, D_d, from the three rows of cooling holes (F, G, H) are compared in Figure 3.8. Note that data from the three holes are shown for their respective locations as was determined from the statistical analyses. Each of the shaped holes evaluated in this study had the same design intent metering diameter. Figure 3.8(a) and Figure 3.8(b) show holes drilled with the high-speed EDM process while Figure 3.8(c) shows holes drilled with the conventional EDM process. These holes are labeled in order starting at the hub of the blade moving upward. While all hole diameters were within tolerance, the conventional EDM holes were typically smaller than the high-speed EDM holes. Additionally, for both hole drill methods, variation in hole size was larger between blades than within a group of holes on the same blade. The variations of diameter for each row are further quantified in Table 3.3.

For the suction side cooling holes (F), shown in Figure 3.8(a), the hole sizes matched well with the flow trends through the suction side of the blade as shown in Figure 3.7. The minimum flow blade had the smallest holes in this region, as well as the lowest flow through the SS. The maximum flow blade had the largest holes, and the highest flow in this region. The metering hole diameter sets the flow through cooling holes so it follows that the flow and hole size should have similar trends as seen in Figure 3.7 and Figure 3.8(a). For all holes in this row, the hole diameters varied from the design diameter by ± 8%. The diameter was more consistent within holes on the same blade than between blades, as outlined in Table 3.3.

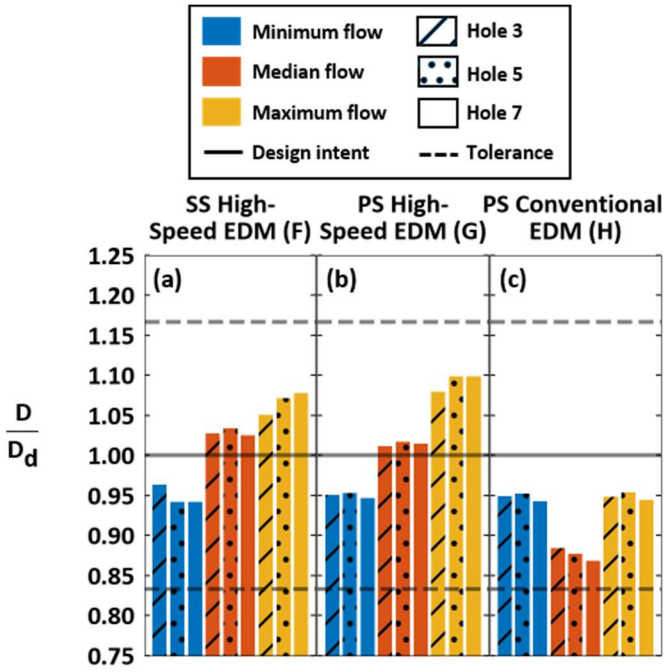

Figure 3.8 Mean diameter in the metering section of holes drilled using high-speed EDM on the (a) suction side (F) and (b) pressure side (G), as well as (c) conventional EDM on the pressure side (H).

Table 3.3 Film Cooling Hole Metering Diameter Variations Normalized by Mean Diameter for Rows F, G, H and from Literature.

	SS High-Speed EDM (F)	PS High-Speed EDM (G)	PS Conventional EDM (H)	Bunker et al. [4]
Normalized mean diameter	1.02	1.02	0.93	–
Normalized diameter range, individual blade row	0.024	0.019	0.018	–
Normalized diameter range, same row between all blades	0.14	0.15	0.09	0.20
Relative variation from design intent diameter	0.94 – 1.08	0.94 – 1.10	0.87 – 0.95	0.9 – 1.1
Relative diameter tolerance	± 0.17	± 0.17	± 0.17	± 0.10

The pressure side holes manufactured using high-speed EDM (G), shown in Figure 3.8(b), had similar trends in hole diameter to the suction side high-speed EDM holes. Hole diameters were consistent for an individual blade with most variation being observed between blades. The maximum flow blade had the largest holes, almost 10% larger than the design intent as seen in

Table 3.3. This maximum blade therefore had the highest flow in this region as shown by Figure 3.7. However, the minimum flow blade had the smallest holes but did not have the lowest flow parameter in the pressure side and tip sections as seen in Figure 3.7.

The holes manufactured using the conventional EDM process for row (H) on the pressure side, shown in Figure 3.8(c), were all undersized relative to the design intent. As mentioned previously, the electrodes made for the conventional EDM process were undersized to account for overburn in the drill process, which left more material than intended. As seen in Table 3.3, the largest hole diameter was undersized by about 5% with the smallest hole being about 13% smaller than design intent diameter. The median flow blade had the smallest hole diameters in this row (H), as well as the lowest flow parameter as seen in Figure 3.7. The maximum flow blade had the highest flow through the pressure side region and larger holes than the median flow blade.

The observed variations in hole size are all within the defined manufacturing tolerances and well within typical tolerance variations in cooling hole sizes for cast turbine components, as indicated by Bunker [4] and shown in Table 3.3. Bunker cited larger manufacturing variations in magnitude and percent deviation than the conventional EDM holes shown above both in actual magnitude and in percent deviation from design intent. These deviations in hole diameter were shown by Bunker to change adiabatic effectiveness by up to 20% [16].

While Bunker's study focused on metering diameters, the NExT blade contains shaped film-cooling holes with additional tolerances. As such, not only the metering diameter is of interest but also the cross-sectional area as a function of hole length. The data from the CT scan for the entire hole area is shown in Figure 3.9 for the three holes on each of the three blades previously discussed. Figure 3.9(a) and Figure 3.9(b) show high-speed EDM holes (G) and conventional EDM holes (H), respectively. Also indicated is the design intent area along with the tolerance throughout the length of the hole. Even when other parameters such as metering diameter and expansion angles may be in tolerance for specific cooling holes, the area at the hole exit is more representative of

whether the hole exit profile meets specifications. While the cross-sectional area was within ± 25% of design intent in the metering section for the high-speed EDM holes, it did not increase as intended along the length of the cooling hole resulting in a smaller exit area. In contrast, the conventional EDM holes were undersized through the entire length of the hole, with a more consistent area between blades.

The lateral and forward expansion angles as shown in Figure 3.3 were measured for each hole as an additional metric for comparison with the area expansion. These angles are shown in Figure 3.10(a) and Figure 3.10(b) for the high-speed EDM holes and conventional EDM holes, respectively. The design intent was 7° for each angle, marked with a black line, while the angle tolerance implied by the profile tolerance discussed in Figure 3.4 is shown in dashed lines. Almost all angles for the high-speed EDM holes were smaller than design intent, which would cause the smaller expansion throughout the length of the hole. While the first lateral expansion angle was closer to 7° for most holes, only hole 7 on the maximum flow blade had a second lateral expansion angle above 7°. The forward expansion angles also tended to be much smaller than intended, especially for the minimum and median flow blades. The profile tolerances defined for these holes allowed variation in hole angle of up to ± 4° depending on the cooling hole shape, meaning that all but two of the forward expansion angles on the minimum flow blade shown in Figure 3.10(a) were within allowed variation. The smaller hole angles for each of these holes led to the decreased area at these hole exits. The process of moving a cylindrical electrode to shape these cooling holes with the high-speed EDM method did not capture the design intent expansion angles as well as the conventional EDM method. Additionally, this method led to more variation in angles between blades and even between rows of cooling holes. While specific cooling holes were inspected with mold impressions by the manufacturer to ensure match to design intent, these inspections were not performed on all batch parts. For this reason, variations in specific holes or parts may pass the manufacturing process undetected.

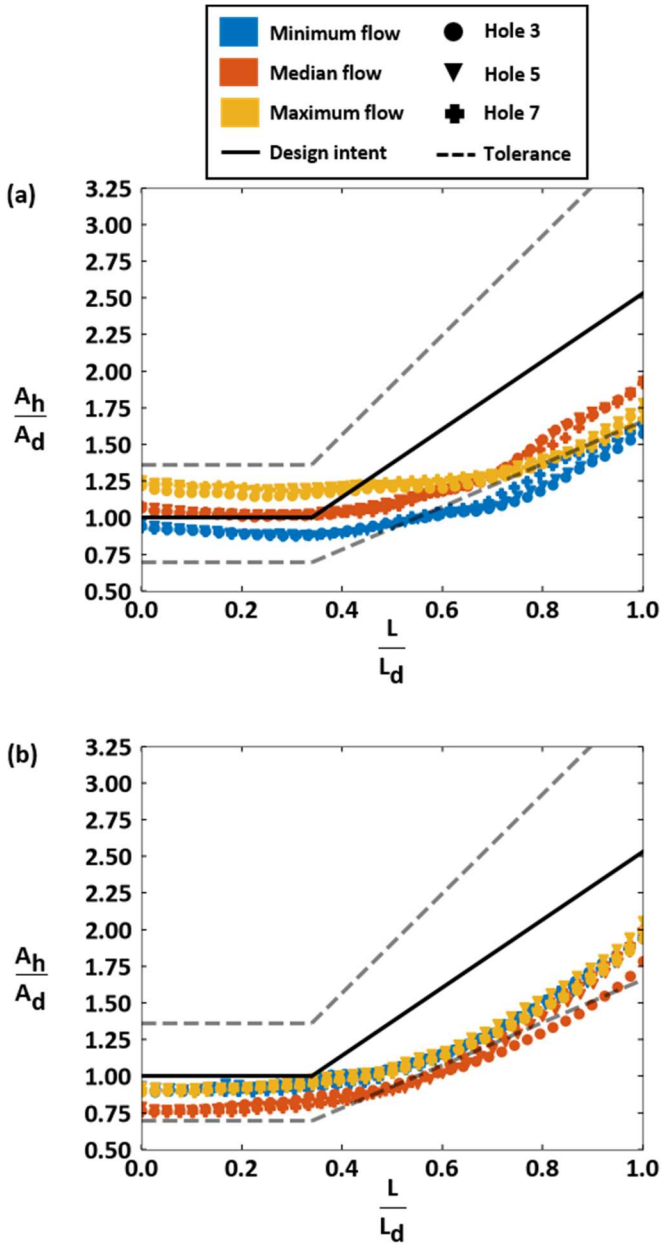

Figure 3.9 Cooling hole area through the length of film cooling holes on the pressure side: (a) high-speed EDM (G); (b) conventional EDM (H) holes.

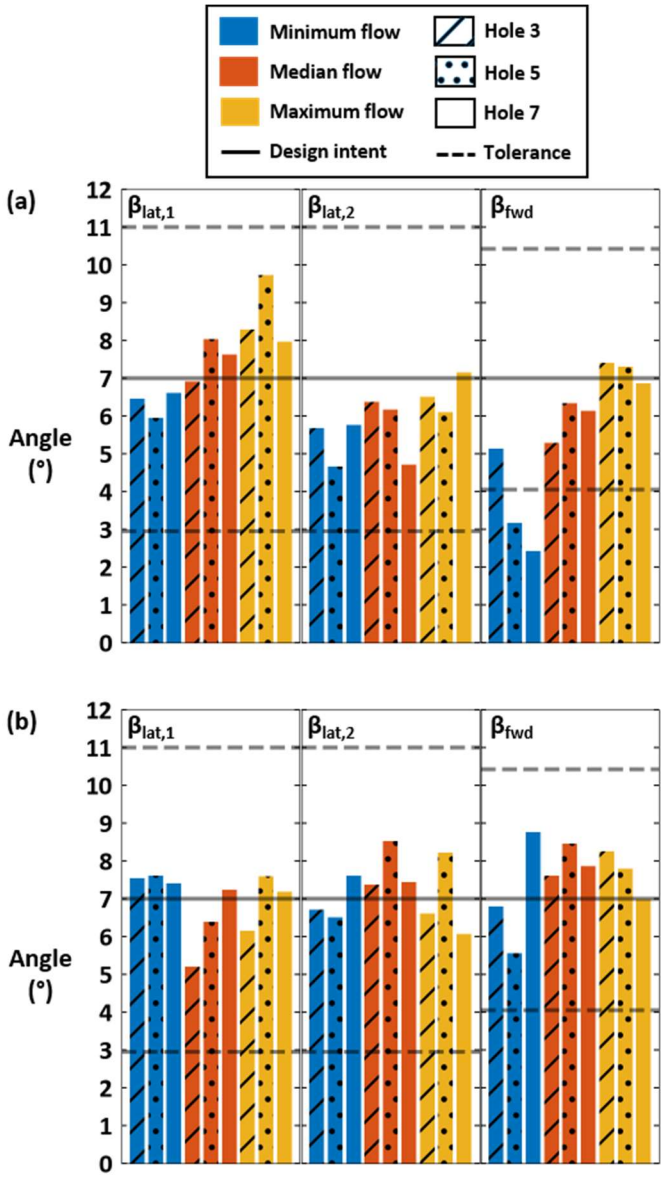

Figure 3.10 Film cooling hole expansion angles for pressure side (a) high-speed EDM (G) and (b) conventional EDM (H) holes.

The conventional EDM holes in Figure 3.10(b) had angles much closer to 7° than the high-speed EDM holes. The smallest angle with the conventional method was 5.2°, compared to angles as small as 2.4° for the high-speed EDM holes. The electrode used to drill the conventional EDM holes had additional tolerance specifications to ensure accurate hole angles, which may have

contributed to the angles for this row measuring closer to design intent. However, because all holes were undersized initially for the conventional EDM, the exit area did not expand to reach the final design intent area. The entire electrode was designed to be undersized to account for overburn, but did not remove enough material and therefore the holes were undersized throughout. Additionally, the hole area did not start expanding at the expected location, indicating that the diffuser section may begin too close to the blade surface. The area of the conventional EDM holes as shown in Figure 3.9 was more consistent between blades than was seen for the high-speed EDM holes, with less variation between the minimum, median, and maximum flow blades.

Although variations in size and angles in these cooling holes led to reduced exit areas, most of the holes shown in Figure 3.9 are in tolerance. Additionally, all but two angles seen in Figure 3.10 are allowed with the profile tolerances of 0.15 mm, as discussed above in Table 3.2 and shown in Figure 3.5. While metering area has the largest impact on limiting flow, reductions in hole exit area and expansion angles have been shown to lower film cooling effectiveness [61]. In the present study, the use of an electrode that matched the hole shape as well as the additional tolerance requirement on the hole angle for the conventional EDM approach led to a much closer match to design intent hole angle than was seen for the high-speed EDM method.

To visually compare the cooling hole shapes for both EDM methods, deviation contours from design intent for film cooling hole rows G and H are shown in Figure 3.11(a) and Figure 3.11(b). Additionally, cross sections of cooling holes drilled with each method are shown in Figure 3.11(c) and Figure 3.11(d). The contours show that the roughness levels within the holes were low relative to the rest of the blade, as the holes were drilled and not additively manufactured. All holes shown had the largest deviations from design intent inside cooling holes. For high-speed EDM the largest deviations occurred at the exit of the hole, while for conventional EDM it occurred in the metering section. A high-speed EDM hole, shown in Figure 3.11(a) and (c), has the characteristic in being warped at the cooling hole exit on the windward side. This deviation led to the blade

surface extending more than 75 µm from the design intent location, which can be seen more clearly in Figure 3.11(c). The undercut feature present at the exit of the cooling hole is an artifact of the high-speed EDM method. In comparison, the hole drilled with the conventional EDM method, shown in Figure 3.11(b) and (d), was closer to the design intent shape particularly at the exit, including angles closer to 7°. Deviation from design intent at the exit was within approximately ± 30 µm around the exit profile, much smaller than the high-speed EDM deviations at the top edge of the hole. The conventional EDM holes in Figure 3.11(d) have a straight exit as designed in the exit region where the high-speed EDM holes are warped. The deviations seen here in hole shape are expected to influence the trajectory of the film cooling jet as it leaves these holes, therefore changing the film cooling performance of these holes during operation.

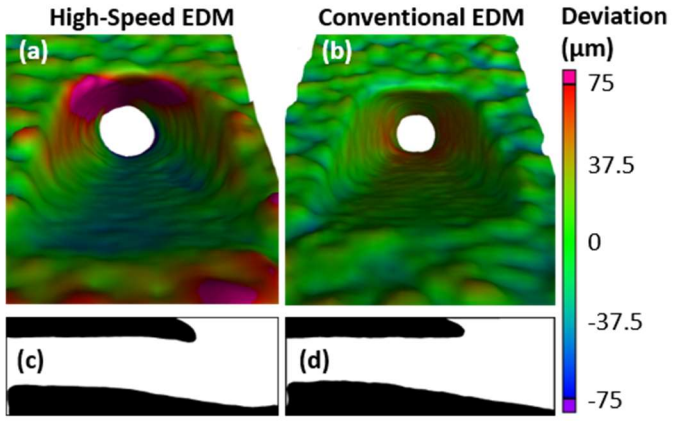

Figure 3.11 Film cooling holes compared to design intent for high-speed EDM (G) (a, c) and conventional EDM (H) (b, d) drill methods.

3.6 Internal Feature Deviations

A variety of internal cooling features on the NExT blades were also evaluated as a part of this study to assess the additive manufacturing technology for cooled turbine blades. The location

of these features is shown in Figure 3.2. Crossover holes are used to meter the flow between regions and are located on internal walls in the leading and trailing edges of the blade. Pin fin arrays, commonly used in the trailing edge, were also used in the NExT blades. Additionally, turbulators on the internal surfaces (also referred to as ribs) were evaluated in the leading edge and trailing edge of the NExT blades. Details on each geometry are presented in Table 3.4.

Table 3.4 Internal Cooling Feature Geometry

	Leading Edge	Trailing Edge
Crossover hole diameter (D_x)	1.0 mm	0.76 mm
Crossover hole spacing (P/D_x)	2.6	4.7
Pin diameter (d)	–	0.89 mm
Pin spacing (s/d)	–	2
Turbulator height (e)	0.46 mm	0.31 mm
Turbulator pitch-to-height ratio (P/e)	5.0	5.8

3.6.1 Crossover Holes

Crossover holes were present at the entry to the leading edge showerhead region and the trailing edge pin fin array, shown in Figure 3.2 as A and B respectively. These holes metered the flow into other sections of the blade. Figure 3.12(a) and Figure 3.12(b) show the minimum area for the crossover holes in the leading edge and trailing edge region, respectively, normalized by the design intent area. Similar to the film cooling holes discussed in earlier sections, slices of CT scan data perpendicular to the flow were used to calculate the area through these holes.

In general, Figure 3.12 shows that all but one of the crossover holes analyzed met tolerance specifications. Because these features were additively manufactured and critical to the performance of the part, they were carefully monitored through AM build trials and iteratively modified through a design for additive manufacturing (DfAM) approach. The measurements reported in Figure 3.12 confirm the success of the DfAM process. In general, the leading edge holes were slightly oversized but closer to the design intent area than the trailing edge holes, which were all undersized.

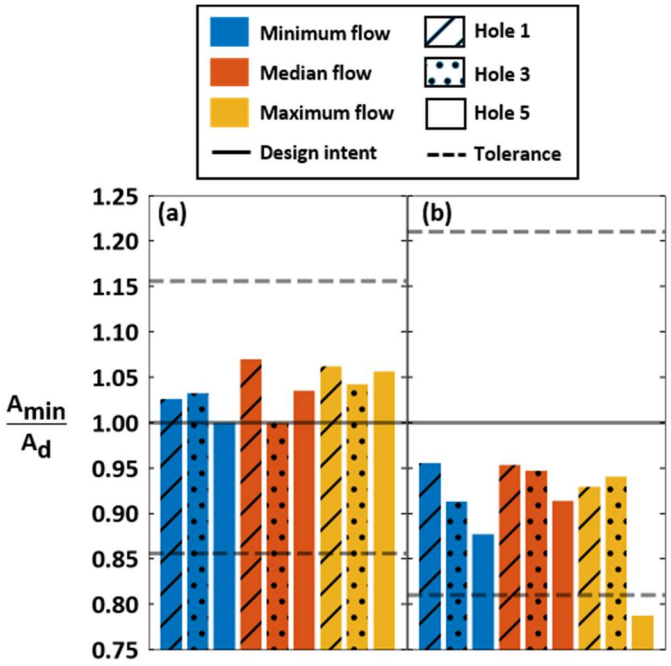

Figure 3.12 Crossover hole minimum area normalized by design intent area for (a) leading edge (A) and (b) trailing edge (B). Solid lines indicate design intent area, while dotted lines indicate minimum and maximum area allowed within tolerances.

Referring to the blade build direction (Figure 3.1) and the blade cross-section (Figure 3.2), the leading edge crossover holes were built perpendicular to the build direction, meaning that one side of the holes was unsupported during the build. Irregularities on these downskin surfaces led to the increased area of these holes by up to 10%, as shown in Figure 3.12(a). Correlating these area observations with flow characteristics, the maximum flow blade had the highest flow through this region as would be expected based on the partial-flow tests summarized in Figure 3.7. Similarly, the minimum flow blade had the smallest hole areas and the lowest flow parameter for the leading edge.

The trailing edge crossover holes were oriented so that no walls inside the holes were unsupported during the build. However, roughness inside the crossover holes led to protrusions that blocked the flow path leading to smaller minimum flow areas on all holes. The trailing edge crossover holes were all undersized, with the smallest hole area only 79% of the design intent area.

Most holes were between 85-95% of the intended size, with the median flow blades having the largest flow area. The median flow blades also had the highest flow in the trailing edge region as seen in Figure 3.7, with a flow reduction of about 10%. The area is reduced by the same amount (10%) as compared to design intent in this region.

3.6.2 Manufacturing Impacts on Flow Distributions

To further synthesize the impacts of the manufacturing variations on the flow distribution, direct connections can be drawn with the partial blade flow measurements. The flow parameter data for crossover holes and film cooling holes as a function of the sum of minimum feature areas are shown in Figure 3.13. The areas plotted here represent the sum of all feature areas presented above, not the entire flow area for a given region. However, the area of the selected individual features was previously shown to be representative of the features in a given location.

Leading edge crossover holes had consistent areas between blades, varying by less than 10% of the design intent area as shown in Figure 3.13. The flow parameter in the leading edge region was lowest for the smallest crossover holes and highest for the largest crossover holes, varying by 16% of the design flow parameter in this region. In the trailing edge region, flow parameter was very similar for all three blades. Crossover hole area was similar between the three blades, again within 10% of the design intent area of each other. The trailing edge flow parameter was also reduced by about 10%, therefore correlating well with the flow area reduction. The crossover holes were additively manufactured with a very consistent cross-sectional area.

The flow parameter through the film cooling holes on the blade varied much more than in the crossover holes as seen in Figure 3.13. The flow parameter for these film cooling hole regions ranged from 110% to 140% of the design intent flow parameter through the suction side, and between 125% and 142% for the pressure side. The film cooling hole areas were lowest for the

lowest flowing blade, and highest for the highest flowing blade. This trend was more apparent for the suction side cooling holes, in which the flow parameter increased linearly along with flow area. Regions with film cooling holes had much larger variations in both flow and hole area than regions where flow was metered by additively manufactured features due to the larger variations in feature size for the EDM methods. However, while the crossover holes discussed above meter all flow through the given regions of the blade, the film cooling hole areas plotted in Figure 3.13 do not represent all holes included in the partial flow data.

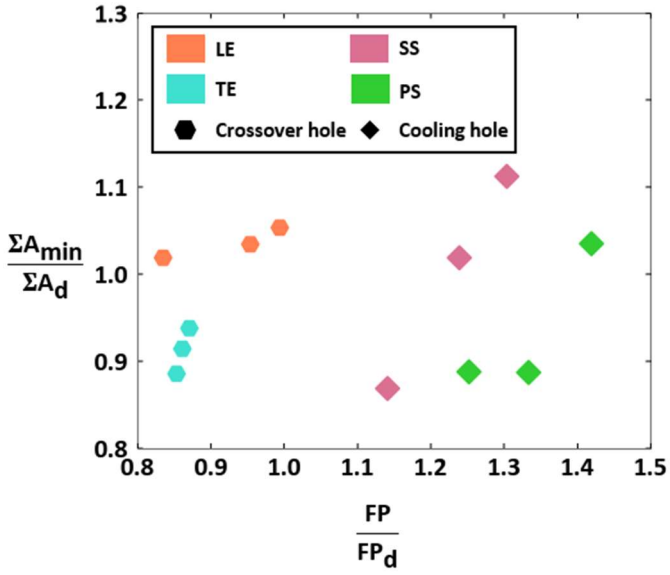

Figure 3.13 Sum of minimum feature area vs. flow parameter, both normalized by design intent, for all measured crossover holes and film cooling holes.

3.6.3 Pin fin Array

The NExT blades contain a pin fin array near the trailing edge, labeled I in Figure 3.2 and described in Table 3.4. A view of the pin fin array generated from CT scans is shown in Figure 3.14. This view is looking towards the trailing edge of the blade with the pressure side surface on

the top of the image and suction side on the bottom of the image. The pin spacing matched the intended values with the maximum pin spacing (s/D) typically varying by ± 10% or less from the design intent. Additionally, the pins were all circular along the entire height as intended and matched the design shape. Only small deviations in pin shape occurred on the downskin surface due to lack of support during the build. In past studies, pins were shown to be non-circular indicating that additive manufacturing is continuing to improve [54–56]. Similar to prior literature, roughness on the pins was much lower than it was on internal walls, which will be discussed further in the upcoming sections.

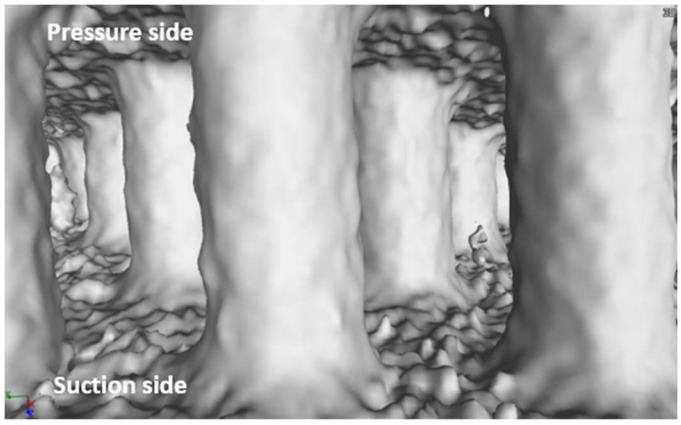

Figure 3.14 CT scan of pin fin array looking towards the trailing edge of the blade, with pressure side of blade at the top of the image and suction side on the bottom.

3.6.4 Internal Wall Turbulator (Rib)

Turbulators, also commonly referred to as ribs in the open literature, are present in many regions throughout the blade internal surfaces. Two specific locations were chosen for evaluation, and the selected regions are denoted with red lines in Figure 3.2 to show where the CT scan slices were collected. The zones are indicated as C on the suction side close to the leading edge and D on the suction side at the trailing edge. The design intent shape of these turbulators was different for each of these regions with the trailing edge turbulators more rounded for the trailing edge (location

D). The leading edge turbulator was designed to be 0.46 mm tall, while the trailing edge turbulator was designed to be smaller at 0.31 mm in height. Additional details on the turbulator design are in Table 3.4. The build orientation in Figure 3.1 shows two green boxes representing the location of the turbulators evaluated. The two slices as shown in Figure 3.2 were located nearly perpendicular to each other. The leading edge turbulators were pointing downward relative to the build direction leading to more unsupported surfaces, whereas the trailing edge turbulators pointed upward.

Comparisons of the design intent (green) and the as-printed part (black) for locations C and D on the median flow blade are shown in Figure 3.15(a) and Figure 3.15(b), respectively. The turbulators in both regions printed close to the design intent with respect to the height. However, both the leading and trailing edge turbulators showed variations from the design intent with respect to the curvature and the width. These deviations were also a result of the build direction. For example, the leading edge turbulators were built facing downward and therefore the bottom of the turbulators (left side in Figure 3.15(a)) were unsupported during the build. As mentioned previously, the greatest driver to pressure loss for turbulators is the spacing and height of the turbulator both of which were captured within approximately ± 10% of design intent for the as-built turbulators. These deviations are in tolerance for both turbulator locations. Previous literature by Taslim et al. [71–73] has shown little change in friction factor as a function of ribbed turbulator height for low blockage ratio turbulators such as those shown here.

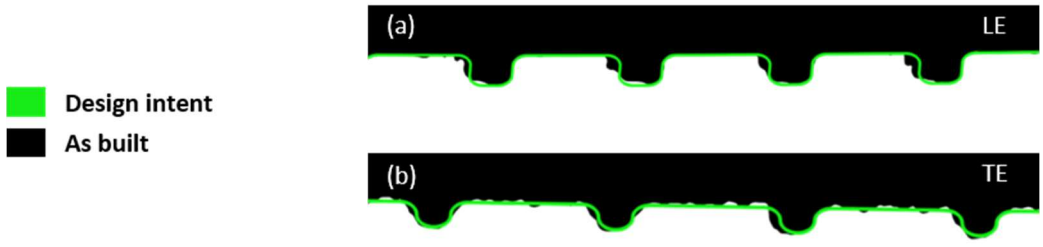

Figure 3.15 Turbulator comparison to design intent on the median blade for (a) location C on the leading edge and (b) location D at the trailing edge.

3.7 Surface Roughness

It is well-known that high surface roughness is often present on metal additively manufactured components. Roughness of these components is typically characterized using arithmetic mean roughness (R_a), which represents the deviations from a reference surface. In this paper, CT scan data were used to quantify the surface roughness by fitting a mean plane to the part surface at the location being analyzed and calculating the deviation of the surface from this plane [54]. While CT scan data are limited by the voxel size, the large features are quantified [74]. A statistical analysis similar to the film cooling hole analysis was carried out to ensure a sufficient number of measurements were used to accurately represent the roughness data with precision uncertainty of 6 μm, which was less than the bias uncertainty.

The measured external and internal roughness levels at seven discrete locations distributed along the NExT blade chord are shown in Figure 3.16. Wall thickness for the given airfoils at the same chord locations is given in Figure 3.16(a). Figure 3.16(b) compares NExT blade roughness to previously reported roughness levels on an independently made additively manufactured vane in a similar orientation [53], as well as on cast airfoils [8]. Figure 3.16(c) shows the external and internal roughness measurements made at approximately the same locations on the blade, on opposite sides of the blade wall. Shaded regions represent the range in roughness between the minimum, median, and maximum flow blades at each location. All NExT measurements were taken at both the 30% and 70% span of the blade for all three blades. No post-processing surface finishing was performed on the NExT blades so all measurements represent as-printed additive surfaces.

External roughness of NExT blades was highest near the trailing edge, particularly on the pressure side as shown in Figure 3.16(b) and Figure 3.16(c). These measurements were above the pin fin array in a region with thin walls, which has been shown to lead to high roughness on additive parts [53]. Moreover, the external roughness was lowest at the leading edge for both span locations.

The leading edge region had thicker walls (1.4 mm for the leading edge relative to 0.7 mm for the trailing edge) and was facing upward during the build, both of which typically lead to lower surface roughness. The suction side of the blade also had lower roughness than the pressure side for most locations due to the build orientation. For regions with similar wall thickness, roughness measurements from the current study matched well with Wildgoose et al. [53]. Where the wall thickness differed, the comparisons with the data presented by Wildgoose et al. showed differences.

External roughness reported for additively manufactured NExT blades is higher than what has been reported previously for cast components, as shown in Figure 3.16(b). Bons et al. [8] found average R_a values for turbine components to be between 3 and 9 μm, while the present study found external roughness values as high as 36 μm. Although both the current study and Bons et al. showed highest roughness values at the pressure side trailing edge, Bons showed relatively uniform roughness across the blade surface.

Internal roughness measured at the same locations and presented in Figure 3.16(c) was higher than the external roughness for almost all portions of the blade. Because roughness was measured throughout the blade, these measurements come from a variety of features on the internal surface. The internal roughness was highest at the trailing edge and leading edge. As mentioned previously, the trailing edge roughness measurements were taken in the pin fin array or trailing edge slots where the walls were thin. These thin walls led to high roughness on both internal and external walls in the TE region. In contrast, the leading edge region has very high internal roughness but low external roughness. The leading edge region was printed nearly parallel to the build plate, with the internal surface facing down and the external surface facing up relative to the build plate. As a result, the selected build orientation that provided a high-quality external aerodynamic shape with limited distortions led to low roughness on the external surface and appreciably higher roughness on the internal surface.

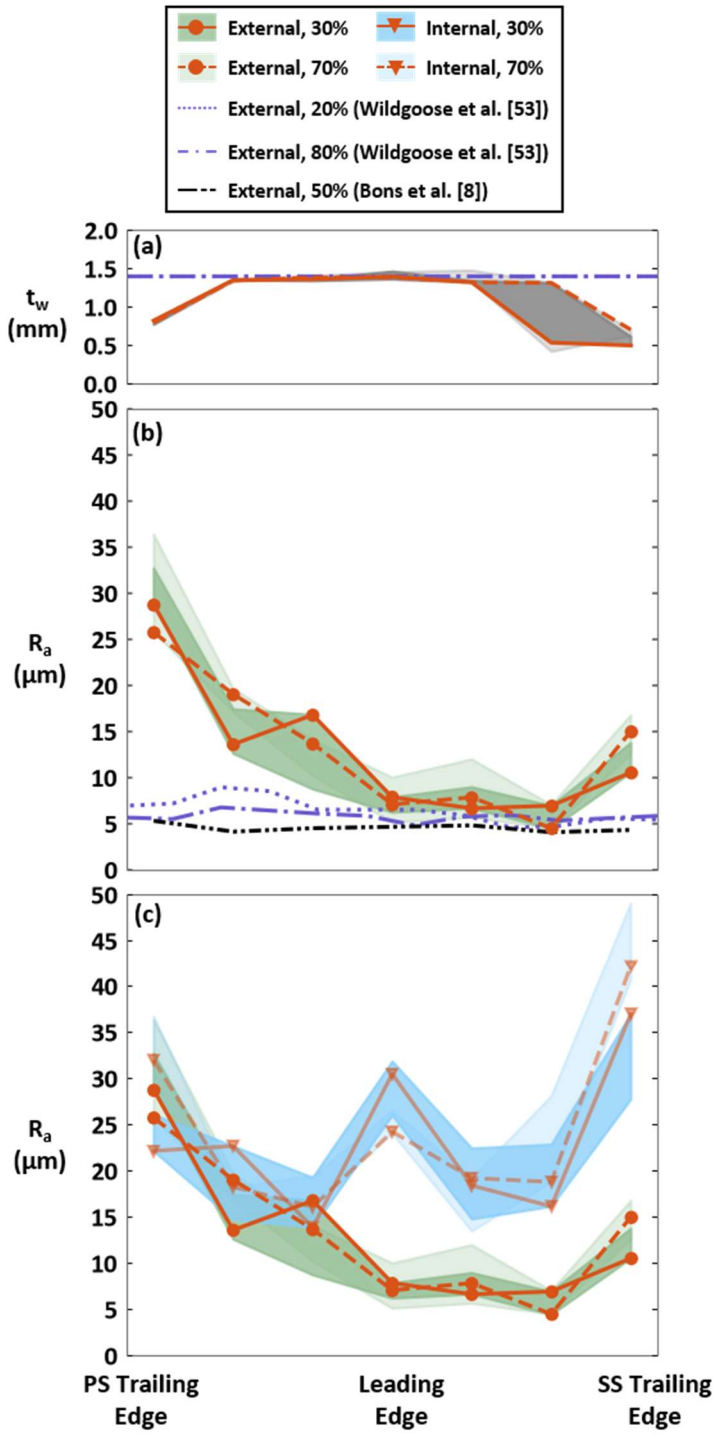

Figure 3.16 (a) Wall thickness (t_w) for blades, (b) measured external roughness compared to literature, and (c) external vs. internal roughness. Solid red lines show the median flow blade, while shaded regions represent the range in roughness values for minimum, median, and maximum flow blades at a given location.

Both internal and external roughness measurements are largely consistent between the three blades within a general range of ± 5 µm at any given location. Additionally, there is no consistent trend in roughness differences between the 30% and 70% spans for either internal or external roughness. Instead of specific location or variation between blades, the data indicate that roughness is more dependent on the features and wall thickness in a given location.

Figure 3.17(a) and Figure 3.17(b) show the roughness of walls between the turbulator regions highlighted in Figure 3.15. The green range in Figure 3.17(a) and Figure 3.17(b) represents previous roughness measurements from literature on additive parts [48,49,54,55,74]. All blades in the trailing edge region and the minimum flow blade in the leading edge region had higher roughness compared to previous literature. The walls were thinner in the trailing edge turbulator walls than in the leading edge region leading to higher roughness in this region. This can be seen in comparing the walls in Figure 3.15(a) and Figure 3.15(b) where surfaces are smoother between the turbulators for the leading edge than the trailing edge. Within a given region roughness was consistent between blades, varying by about three microns or less.

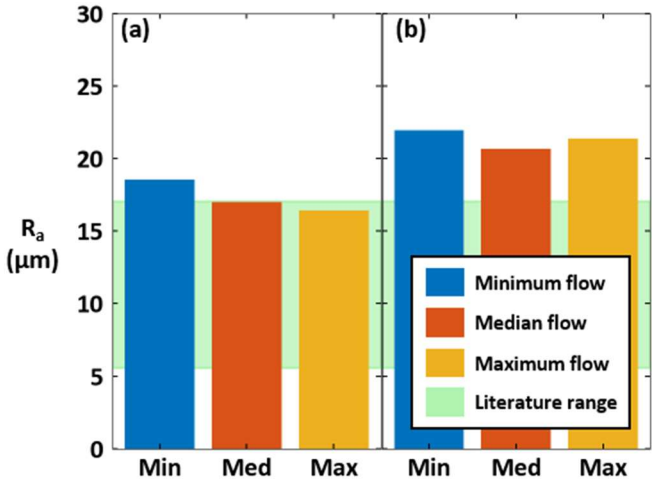

Figure 3.17 Internal wall roughness between turbulators at the blade (a) leading edge (D) and (b) trailing edge (C), with range of roughness found in literature shown in green [49,53–55,74].

Additionally, roughness was measured on the walls of the pins as well as the internal walls in the pin fin array as shown in Figure 3.18(a-c). Roughness values from Corbett et al. [56] are shown in light blue for pin surfaces (Figure 3.18(a)) and dark blue for internal walls (Figure 3.18(b-c)). Roughness measurements for the current study were lower than previous literature both on pin surfaces and internal walls due to differences in wall thickness, with the coupons in Corbett et al. having thinner walls than the current study. Additionally, roughness on pin internal walls was higher than on walls between turbulators as shown in Figure 3.17. The roughness was almost twice as high on the internal walls as it was on the pins themselves. The internal walls were thinner than the pin fins in this region, likely causing the difference in roughness. This trend has been seen in past literature of additively manufactured pin fins with wall roughness sometimes as much as 8.5 times higher than the pin roughness [56]. To see this trend more clearly, the CT scan of the pin fin array shown in Figure 3.14 displays the smooth pin surfaces in comparison to the rough internal walls.

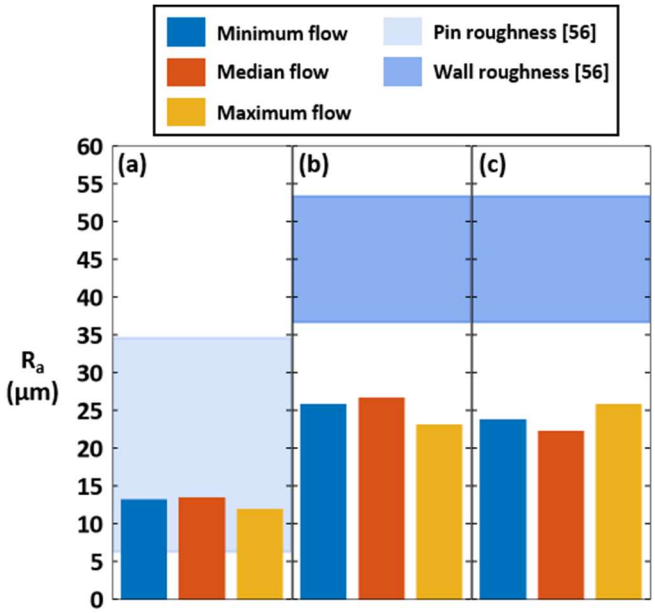

Figure 3.18 Roughness on (a) pin surfaces, (b) suction side internal wall, and (c) pressure side internal wall in the trailing edge pin fin array (I), with the range of pin and internal wall roughness from literature shown in blue [56].

3.8 Summary of Manufacturing Impacts

Considering machined film cooling holes, two EDM methods were evaluated in the current study both of which led to undersized hole exit areas. One difference, however, was that the high-speed EDM holes had more variation in diameter and typically showed reduced hole expansion angles relative to the conventional EDM holes, which is expected to result in reduced film cooling spreading. Furthermore, high-speed EDM processes led to undercut surfaces with the formation of a "lip" that differs from using conventional EDM electrodes. The conventional EDM holes had expansion angles much closer to design intent than did the high-speed EDM holes, but consistently undersized metering areas. Although the tolerances that were specified for the NExT blades were similar to what would be used with production-grade airfoils, diffuser angles can differ significantly from the design intent when profile tolerances are used. With this in mind, the selection of hole drill methods is an important area for continued research and development.

The use of additive manufacturing for the NExT program was able to manufacture commonly used cooling features in a turbine airfoil that met the design intent. All measured deviations from the design fell within defined tolerances that are realistic for engine manufacturing, with the exception of one trailing edge crossover hole. The build direction and wall thickness had the largest impacts on feature quality and surface roughness. Downskin surfaces showed the most variation between parts and the thinnest walls produced the highest roughness. While the trailing edge of the blade was oriented facing downwards during manufacturing for the current study to ensure a best fit of external aerodynamic shape, this build orientation could be modified for future work to further refine internal surface quality. Following a comparison with literature, roughness was much higher for the NExT AM blades than for cast blades. Although it was not performed for these specific airfoils for purposes of fully assessing the additively manufactured parts, external surface finishing could be implemented as a post-processing step for future airfoils. Regardless, the

use of additive manufacturing provides significant flexibility for current and future research to investigate novel cooling technologies for engine applications at a rapid pace and with a reduced cost.

3.9 Conclusions

This study investigated the manufacturing impacts resulting from additively manufactured cooled turbine blades for the NExT program. A set of blades was printed and flow tested with three representative blades chosen for detailed analyses. Film cooling holes on the blades were drilled separately using two different EDM methods: conventional and high-speed. These blades were compared to the design intent using CT scans to determine the levels of variation due to the additive process. Finally, variations in the flow were correlated with the specific manufacturing deviations in several regions of the blades.

The full blade flow parameter for the entire set of NExT blades varied by no more than 10% from that specified for the design pressure ratio. Flow through individual regions of the blade varied from the design flow while still adding up to the intended flow parameter for the full blade flow. The highest flow region, the pressure side and tip, was measured to flow up to 40% higher than the design intent flow. All three blades underflowed in the trailing edge region, with reductions in flow of about 10% from the design intent flow. The maximum variation in flow parameter between blades was consistent for the leading edge, suction side, pressure side and tip regions.

The high-speed EDM holes were close to the design intent diameter in the metering section of the hole, but had reduced exit area and expansion angles smaller than 7° resulting in a reduced lateral spread. The conventional EDM holes were close to the design expansion angles, but had slightly undersized metering diameter. Both drilling methods resulted in undersized diffuser exits but for different reasons. Given that these EDM methods are common in gas turbine manufacturing

and independent of whether the airfoils are produced by additive manufacturing or casting, cooling holes on engine hardware likely deviate from their design intent in similar ways to what has been shown in this study.

Overall, cooling features printed close to design intent with relatively small variations between blades. Features such as turbulators and pin fins matched the design intent shape, but had high roughness on downskin surfaces. The roughness on the internal and external blade surfaces was higher than most literature on cast turbine components, but more closely represented prior additively manufactured components. The largest deviations of roughness relative to prior literature were for downskin surfaces and in regions with the thinnest walls such as the trailing edge.

This study provides a look into how the additive manufacturing process can affect a variety of internal cooling features of turbine blades, while also analyzing two hole drill methods and their effect on film cooling hole geometries. Additive manufacturing was able to produce the intended blade with desired cooling designs providing a powerful vehicle for research and development programs to evaluate new hardware sets with reduced manufacturing costs and lead times relative to cast airfoils. This knowledge provides an understanding of both traditional and additive manufacturing processes for turbine designers. The impacts of these blade deviations on turbine heat transfer will be studied in subsequent papers. Additionally, these blades serve as a baseline for future research collaboration between academia, industry, and government to advance cooling technology for future gas turbines.

Chapter 4

Conclusions and Recommendations

As turbine inlet temperatures continue to rise in an effort to increase efficiency, it is necessary for turbine designers to understand how cooling features affect surface temperatures to assess durability of components. Additionally, the impact of manufacturing variations and operational deterioration on the temperature and performance of these parts must be well understood. This thesis has investigated the impacts of manufacturing methods and engine operation on the geometry, flow, and cooling effectiveness of true scale turbine blades.

The first study of this thesis focused on engine-operated turbine from environments around the world. Four sets of blades were tested: baseline blades, high run time blades operated in a benign environment, low run time blades in a harsh environment, and high run time blades in a harsh environment. Flow parameter measurements taken with a benchtop rig showed reduced flow compared to the baseline for all engine operated blades, with the harsh operator high run time blades having both the largest reduction and largest variations in flow parameter. In the tip trailing edge region, both harsh operators had very similar cooling effectiveness between 80% and 90% of the baseline blade maximum value. The benign operator blade with the highest run time had higher cooling effectiveness in this region for both high and low blade cooling flow rates due to lower levels of deterioration in this region. Film cooling trajectories were imaged using infrared thermography, and were shown to detach from the blade surface for most of the engine run blades leading to much lower cooling effectiveness behind the holes. To compare the impact of these flow and cooling variations at true operational conditions, the cooling effectiveness measurements were scaled to NASA E3 engine conditions to predict engine temperatures. While existing lifing models were able to predict the surface temperature increase for the benign operator blades, the harsh

operator blades had much shorter lives than expected for the surface temperature increase measured. This research emphasizes the importance of environmental effects on blade lifing.

The second study analyzed the geometry and flow of additively manufactured turbine blades with EDM film cooling holes. While the full blade flow measurements matched well with design intent, partial blade flow varied more significantly. Individual regions of blades varied in flow by up to 40% from design flow parameter. Flow measurements were used to select a minimum, median, and maximum flow blade for further analysis using CT scans. Shaped film cooling holes manufactured using high-speed EDM were close to design intent in the metering section, but had smaller expansion angles than intended and were therefore undersized at the hole exit. In contrast, conventional EDM holes were undersized throughout the entire length of the hole, even though their expansion angles matched design intent more closely. For the film cooling holes as well as internal cooling features such as crossover holes, the minimum flow areas correlated with the amount of flow through a given region. Ribbed turbulators and pins both built close to the design intent, with high roughness on internal walls in both regions. Roughness on the external surface was typically higher than roughness on the internal surface, with both levels peaking for regions with the thinnest walls and on downskin surfaces. This study emphasizes the feasibility of using additive manufacturing to investigate novel cooling designs, while also exploring the variations of geometry allowed within typical turbine component tolerances.

This research provides a new understanding of the effects of turbine blade variations due to either environmental deterioration or manufacturing methods on flow and cooling performance. The methods and results here can be used by gas turbine designers to predict the impacts of these variations on true engine components.

4.1 Recommendations for Future Work

Future work can be performed to further investigate the effects of environmental and manufacturing variations on turbine performance. While blockages within cooling holes were suspected to be contributors to the reduced flow and cooling effectiveness of engine run blades, a more detailed study of the blades would provide insight into the exact types and locations of blockages. This information would improve the understanding of how particulates build up inside a blade along with how those buildups affect the flow and temperature, which together would greatly aid in understanding life of hot section components. Additionally, studying blades that have operated in additional locations around the world with different types of degradation than those studied in this thesis would provide a more complete picture of how components deteriorate during operation.

While the geometry and flow of a set of additively manufactured NExT blades was investigated, future work should focus on quantifying the performance of this blade set. The geometric analysis outlined in this thesis could be used to analyze the cooling effectiveness and efficiency of the components. A similar analysis to that performed on the NExT blades in this thesis could also be done for the NExT vanes, including the proposed future research on performance at engine-relevant conditions. Additionally, the same blade geometry could be manufactured with different methods to identify how specific features are impacted. While this thesis studied additively manufactured blades, a comparison to cast components would allow for more definitive conclusions on how well the blades used represent true engine geometries.

References

[1] Bunker, R. S., 2017, “Evolution of Turbine Cooling,” GT2017-63205.

[2] Saravanamuttoo, H., Rogers, G., Cohen, H., and Straznicky, P., 2009, *Gas Turbine Theory*, Pearson Education Limited.

[3] Meher-Homji, C. B., and Gabriles, G., 1998, “Gas Turbine Blade Failures - Causes, Avoidance, and Troubleshooting,” Proceedings of the 27th Turbomachinery Symposium, pp. 129–180.

[4] Bunker, R. S., 2009, “The Effects of Manufacturing Tolerances on Gas Turbine Cooling,” J. Turbomach, **131**(4), p. 041018.

[5] Knisely, B. F., Berdanier, R. A., Wagner, J. H., Thole, K. A., Arisi, A. N., and Haldeman, C. W., 2023, “Effects of Part-to-Part Flow Variations on Overall Effectiveness and Life of Rotating Turbine Blades,” Journal of Turbomachinery, **145**(6), p. 061016.

[6] Hamed, A., Tabakoff, W. C., and Wenglarz, R. V., 2006, “Erosion and Deposition in Turbomachinery,” J. Propuls. Power, **22**(2), pp. 350–360.

[7] Bogard, D. G., Schmidt, D. L., and Tabbita, M., 1996, “Characterization and Laboratory Simulation of Turbine Airfoil Surface Roughness and Associated Heat Transfer,” 96-GT-386.

[8] Bons, J. P., Taylor, R. P., McClain, S. T., and Rivir, R. B., 2001, “The Many Faces of Turbine Surface Roughness,” GT-2001-0163.

[9] Ekkad, S. V., and Han, J. C., 2000, “Film Cooling Measurements on Cylindrical Models with Simulated Thermal Barrier Coating Spallation,” J. Thermophys. Heat Transfer, **14**(2), pp. 194–200.

[10] Ekkad, S., and Han, J.-C., 1997, "Detailed Heat Transfer Distributions on a Cylindrical Model with Simulated TBC Spallation," Proceedings of the 35th Aerospace Sciences Meeting and Exhibit, pp. 97–0595.

[11] Lawson, S. A., and Thole, K. A., 2011, "Effects of Simulated Particle Deposition on Film Cooling," J. Turbomach, **133**(2), p. 021009.

[12] Sundaram, N., and Thole, K. A., 2007, "Effects of Surface Deposition, Hole Blockage, and Thermal Barrier Coating Spallation on Vane Endwall Film Cooling," J. Turbomach, **129**(3), pp. 599–607.

[13] Singh, S., and Tafti, D., 2015, "Particle Deposition Model for Particulate Flows at High Temperatures in Gas Turbine Components," Int. J. of Heat Fluid Flow, **52**, pp. 72–83.

[14] Hamed, A. A., Tabakoff, W., Rivir, R. B., Das, K., and Arora, P., 2005, "Turbine Blade Surface Deterioration by Erosion," J. Turbomach, **127**, pp. 445–452.

[15] DeShong, E. T., Berdanier, R. A., and Thole, K. A., 2023, "Predictive Modeling of Local Film-Cooling Flow on a Turbine Rotor Blade," J. Turbomach, **145**(4), p. 041014.

[16] Bunker, R. S., 2000, "Effect of Partial Coating Blockage on Film Cooling Effectiveness," GT-2000-0244.

[17] Whitfield, C. A., Schroeder, R. P., Thole, K. A., and Lewis, S. D., 2015, "Blockage Effects From Simulated Thermal Barrier Coatings for Cylindrical and Shaped Cooling Holes," J. Turbomach, **137**, p. 091004.

[18] Ramirez Velasco, J. H., Petrosky, K., Kilaz, G., Kenttämaa, H., and Trice, R. W., 2021, "Thermochemical Interaction of Biofuel Impurities with Yttria-Stabilized Zirconia Thermal Barrier Coatings," Ceramics International, **47**(17), pp. 24675–24682.

[19] Murugan, M., Ghoshal, A., Walock, M., Nieto, A., Bravo, L., Barnett, B., Pepi, M., Swab, J., Pegg, R. T., Rowe, C., Zhu, D., and Kerner, K., 2017, "Microstructure Based Material-Sand Particulate Interactions and Assessment of Coatings for High Temperature Turbine Blades," GT2017-64051.

[20] Mund, M. G., and Guhne, H., 1970, "Gas Turbines — Dust — Air Cleaners: Experience and Trends," 70-GT-104.

[21] Murugan, M., Ghoshal, A., Walock, M. J., Barnett, B. B., Pepi, M. S., and Kerner, K. A., 2017, "Sand Particle-Induced Deterioration of Thermal Barrier Coating on Gas Turbine Blades," Adv. Aircraft Spacecraft Science, **4**(1), pp. 37–52.

[22] Sidwell, V., and Darmofal, D., 2003, "Probabilistic Analysis of a Turbine Cooling Air Supply System: The Effect on Airfoil Oxidation Life," GT-2003-38119.

[23] Bogard, D. G., and Thole, K. A., 2006, "Gas Turbine Film Cooling," J. Propuls. Power, **22**(2), pp. 249–270.

[24] Han, J.-C., and Wright, L. M., 2006, "Enhanced Internal Cooling of Turbine Blades and Vanes," *Gas Turbine Handbook*, Department of Energy, National Energy Technology Laboratory, Morgantown, WV, pp. 321–352.

[25] Bunker, R. S., Dees, J. E., and Palafox, P., 2014, "Impingement Cooling in Gas Turbines: Design, Applications, and Limitations," *Impingement Jet Cooling in Gas Turbines*, WIT Press, pp. 1–32.

[26] Reyhani, M. R., Alizadeh, M., Fathi, A., and Khaledi, H., 2013, "Turbine Blade Temperature Calculation and Life Estimation – A Sensitivity Analysis," Propuls. Power Research, **2**(2), pp. 148–161.

[27] Halila, E. E., Lenahan, D. T., and Thomas, T. T., 1982, *Energy Efficient Engine High Pressure Turbine Test Hardware Detailed Design Report*, NASA Report No. CR-17955.

[28] Lemieux, D. H., 2005, *On-Line Thermal Barrier Coating Monitoring for Real-Time Failure Protection and Life Maximization*, US Department of Energy Technical Report.

[29] Markham, J., Cosgrove, J., Scire, J., Haldeman, C., and Agoos, I., 2014, "Aircraft Engine-Mounted Camera System for Long Wavelength Infrared Imaging of In-Service Thermal Barrier Coated Turbine Blades," Rev. Scientific Instruments, **85**(12), p. 124902.

[30] Sisti, M., Falsetti, C., Beard, P., and Chana, K., 2021, "Infrared Temperature Measurements on High Pressure Turbine Blades in the Oxford Turbine Research Facility: Calibration and Image Processing Techniques," Proceedings of the 14th European Conference on Turbomachinery Fluid Dynamics & Thermodynamics, ETC2021-780.

[31] Christensen, L., Celestina, R., Sperling, S., Mathison, R., Aksoy, H., and Liu, J., 2020, "Infrared Temperature Measurements of the Blade Tip for a Turbine Operating at Corrected Engine Conditions," J. Turbomach, **143**, p. 101005.

[32] Lazzi Gazzini, S., Schädler, R., Kalfas, A. I., and Abhari, R. S., 2017, "Infrared Thermography with Non-Uniform Heat Flux Boundary Conditions on the Rotor Endwall of an Axial Turbine," Meas. Sci. Technol., **28**(2), p. 025901.

[33] Michaud, M., Chowdhury, N., and Povey, T., 2023, "Experimental Study of Impact of In-Service Deterioration on Thermal Performance of High-Pressure Nozzle Guide Vanes," J. Turbomach, **145**(2), pp. 1–17.

[34] Barringer, M., Coward, A., Clark, K., Thole, K. A., Schmitz, J., Wagner, J., Alvin, M. A., Burke, P., and Dennis, R., 2014, "The Design of a Steady Aero Thermal Research

Turbine (START) for Studying Secondary Flow Leakages and Airfoil Heat Transfer," GT-2014-25570.

[35] Berdanier, R. A., Monge-Concepción, I., Knisely, B. F., Barringer, M. D., Thole, K. A., and Grover, E. A., 2019, "Scaling Sealing Effectiveness in a Stator–Rotor Cavity for Differing Blade Spans," J. Turbomach, **141**(5), p. 051007.

[36] Knisely, B. F., Berdanier, R. A., Thole, K. A., Haldeman, C. W., Markham, J. R., Cosgrove, J. E., Carlson, A. E., and Scire, J. J., 2021, "Acquisition and Processing Considerations for Infrared Images of Rotating Turbine Blades," J. Turbomach, **143**(4), p. 041013.

[37] Moffat, R. J., 1988, "Describing the Uncertainties in Experimental Results," Exp. Therm. Fluid Sci., **1**(1), pp. 3–17.

[38] Thole, K. A., Barringer, M., Berdanier, R. A., Fishbone, S., Wagner, J., Dennis, R., Black, J., Burke, P., Straub, D., O'Neill, F., Stimpson, C., Riahi, A., Aggarwala, A., Bradshaw, S., Kohli, A., Mongillo, D., Praisner, T., Rodriguez, J., Fox, M., and Kim, Y., 2021, "Defining a Testbed for the U.S. Turbine Industry: The National Experimental Turbine (NExT)," AIAA 2021-3489.

[39] Krewinkel, R., Such, A., De La Torre, A. O., Wiedermann, A., Castillo, D., Rodriguez, S. A., Schleifenbaum, J. H., and Blaswich, M., 2020, "Design and Characterization of Additively Manufactured NGVs Operated in a Small Industrial Gas Turbine," Int. J. Gas Turbine Propulson and Power Systems, **11**(4), pp. 36–44.

[40] Lindbäck, M., Frankolin, K., Tuneskog, E., Karlsson, B., and Wang, L., 2023, "Development and Validation Under Engine Operation Environment of Additively Manufactured Hot Turbine Parts," GT-2023-103771.

[41] Cecconi, M., and Giovannetti, I., 2023, “Development of Additive Manufacturing Gas Turbine Hot Gas Path Vanes at Baker Hughes,” GT-2023-103043.

[42] Gibson, T., and Romer, T., 2017, “Additive Advantage,” Mechanical Engineering Magazine, **139**(12), p. 35.

[43] Kirka, M., Ryan, D., and Adair, D., 2020, *Full Scale Engine Demonstration of Additively Manufactured High Gamma Prime Turbine Blade*, ORNL CRADA NFE 19-07619.

[44] Magerramova, L., Vasilyev, B., and Kinzburskiy, V., 2016, “Novel Designs of Turbine Blades for Additive Manufacturing,” GT-2016-56084.

[45] Thole, K. A., Lynch, S. P., and Wildgoose, A. J., 2021, “Review of Advances in Convective Heat Transfer Developed through Additive Manufacturing,” *Adv. Heat Transf.*, Elsevier, pp. 249–325.

[46] McCormack, K. E., Gailey, N. L., Berdanier, R. A., Barringer, M. D., and Thole, K. A., 2023, “Quantifying Part-to-Part Flow Variations and Cooling Effectiveness in Engine-Run Blades,” GT-2023-103065.

[47] Snyder, J. C., and Thole, K. A., 2020, “Tailoring Surface Roughness Using Additive Manufacturing to Improve Internal Cooling,” J. Turbomach, **142**(7), p. 071004.

[48] Wildgoose, A. J., and Thole, K. A., 2023, “Heat Transfer and Pressure Loss of Additively Manufactured Internal Cooling Channels With Various Shapes,” J. Turbomach, **145**(7), p. 071011.

[49] Stimpson, C. K., Snyder, J. C., Thole, K. A., and Mongillo, D., 2017, “Scaling Roughness Effects on Pressure Loss and Heat Transfer of Additively Manufactured Channels,” J. Turbomach, **139**(2), p. 021003.

[50] Wu, Z., Narra, S. P., and Rollett, A., 2020, "Exploring the Fabrication Limits of Thin-Wall Structures in a Laser Powder Bed Fusion Process," Int J Adv Manuf Technol, **110**(1–2), pp. 191–207.

[51] Jamshidinia, M., and Kovacevic, R., 2015, "The Influence of Heat Accumulation on the Surface Roughness in Powder-Bed Additive Manufacturing," Surface Topography: Metrology and Properties, **3**(1).

[52] Vasinonta, A., Beuth, J. L., and Ong, R., 2001, "Melt Pool Size Control in Thin-Walled and Bulky Parts via Process Maps," *International Solid Freeform Fabrication Symposium*.

[53] Wildgoose, A. J., A. Thole, K., Subramanian, R., Kersting, L., and Kulkarni, A., 2023, "Impacts of the Additive Manufacturing Process on the Roughness of Engine Scale Vanes and Cooling Channels," J. Turbomach, **145**(4), p. 041013.

[54] Ferster, K. K., Kirsch, K. L., and Thole, K. A., 2018, "Effects of Geometry, Spacing, and Number of Pin Fins in Additively Manufactured Microchannel Pin Fin Arrays," J. Turbomach, **140**(1), p. 011007.

[55] Kirsch, K. L., and Thole, K. A., 2017, "Pressure Loss and Heat Transfer Performance for Additively and Conventionally Manufactured Pin Fin Arrays," International Journal of Heat and Mass Transfer, **108**(B), pp. 2502–2513.

[56] Corbett, T. M., Thole, K. A., and Bollapragada, S., 2023, "Impacts of Pin Fin Shape and Spacing on Heat Transfer and Pressure Losses," J. Turbomach, **145**(5), p. 051014.

[57] Krille, T., Poser, R., Von Wolfersdorf, J., and Henze, M., 2023, "An Experimental Investigation on Pressure Loss and Local Heat Transfer Characteristics in Additively Manufactured Ribbed Cooling Configurations," Int. J. Heat Mass Transfer, **202**, p. 123668.

[58] Stimpson, C. K., Snyder, J. C., Thole, K. A., and Mongillo, D., 2018, "Effectiveness Measurements of Additively Manufactured Film Cooling Holes," J. Turbomach, **140**(1), p. 011009.

[59] Snyder, J. C., and Thole, K. A., 2020, "Performance of Public Film Cooling Geometries Produced Through Additive Manufacturing," J. Turbomach, **142**(5), p. 051009.

[60] Goldstein, R. J., Eckert, E. R. G., and Burggraf, F., 1974, "Effects of Hole Geometry and Density on Three-Dimensional Film Cooling," Int. J. Heat Mass Transfer, **17**(5), pp. 595–607.

[61] Bunker, R. S., 2005, "A Review of Shaped Hole Turbine Film-Cooling Technology," J. Heat Transfer, **127**(4), pp. 441–453.

[62] Haydt, S., Lynch, S., and Lewis, S., 2017, "The Effect of a Meter-Diffuser Offset on Shaped Film Cooling Hole Adiabatic Effectiveness," J. Turbomach, **139**(9), p. 091012.

[63] Haydt, S., Lynch, S., and Lewis, S., 2018, "The Effect of Area Ratio Change Via Increased Hole Length for Shaped Film Cooling Holes With Constant Expansion Angles," Journal of Turbomachinery, **140**(5), p. 051002.

[64] Jones, F. B., Fox, D. W., Oliver, T., and Bogard, D. G., 2021, "Parametric Optimization of Film Cooling Hole Geometry," GT-2021-59326.

[65] Schroeder, R. P., and Thole, K. A., 2022, "Adiabatic Effectiveness Measurements for a Baseline Shaped Film Cooling Hole," J. Turbomach, **144**(12), p. 121003.

[66] Jameson, E. C., 2001, *Electrical Discharge Machining*, Society of Manufacturing Engineers, Dearborn, MI.

[67] Forrester, R. E., Kimberlin, D. E., and Lang, G. J., "Complex Hole Shaping."

[68] Figliola, R. S., and Beasley, D. E., 2014, *Theory and Design for Mechanical Measurements*, John Wiley & Sons, Inc., USA.

[69] Becker, B., Maier, D., and Reinhart, C., 2012, "Computer Tomography Has Arrived in Automated Inspection Processes, Combining Material and Geometry Analyses," Proceedings of 18th World Conference on Non-Destructive Testing.

[70] Veley, E. M., Thole, K. A., Furgeson, M. T., and Bogard, D. G., 2023, "Printability and Overall Cooling Performance of Additively Manufactured Holes With Inlet and Exit Rounding," Journal of Turbomachinery, **145**(3), p. 031017.

[71] Taslim, M. E., and Lengkong, A., 1998, "45 Deg Staggered Rib Heat Transfer Coefficient Measurements in a Square Channel," Journal of Turbomachinery, **120**(3), pp. 571–580.

[72] Taslim, M. E., and Lengkong, A., 1998, "45° Round-Corner Rib Heat Transfer Coefficient Measurements in a Square Channel," 98-GT-176.

[73] Taslim, M. E., and Wadsworth, C. M., 1997, "An Experimental Investigation of the Rib Surface-Averaged Heat Transfer Coefficient in a Rib-Roughened Square Passage," Journal of Turbomachinery, **119**(2), pp. 381–389.

[74] Snyder, J. C., Stimpson, C. K., Thole, K. A., and Mongillo, D. J., 2015, "Build Direction Effects on Microchannel Tolerance and Surface Roughness," J. Mech. Design, **137**(11), p. 111411.